Probing Relaxation Dynamics in Five-Coordinate Dysprosium Single-Molecule Magnets

Vijay S Parmar, Fabrizio Ortu, Xiaozhou Ma, Nicholas F Chilton, Rodolphe Clérac, David P Mills, Richard E P Winpenny

Probing Relaxation Dynamics in Five-Coordinate Dysprosium Single-Molecule Magnets

Vijay S. Parmar,[a] Fabrizio Ortu,[a] Xiaozhou Ma,[b] Nicholas F. Chilton,[a] Rodolphe Clérac,*[b] David P. Mills,*[a] and Richard E. P. Winpenny*[a]

Abstract: A new family of five-coordinate lanthanide single-molecule magnets (Ln SMMs) $[Dy(Mes^*O)_2(THF)_2X]$ (Mes^* = 2,4,6-tri-tert-butylphenyl; X = Cl, **1**; Br, **2**; I, **3**) is reported with energy barriers to magnetic reversal > 1200 K. The five-coordinate Dy^{III} ions have distorted square pyramidal geometries, with halide anions on the apex, and two Mes*O ligands mutually *trans*- to each other, and the two THF molecules forming the second *trans*- pair. These geometrical features lead to a large magnetic anisotropy in these complexes along the *trans*-Mes*O direction. QTM and Raman relaxation times are enhanced by varying the apex halide from Cl to Br to I, or by dilution in a diamagnetic yttrium analogue.

Single-molecule magnets (SMMs) show slow relaxation of magnetisation under certain conditions; these have received huge interest in the last 25 years due to their potential applications in quantum computing, molecular spintronics and ultra-high-density storage.[1,2] For technological applications, it is important to determine the highest temperature at which a SMM can retain its magnetisation,[1] and to understand the multiple relaxation mechanisms, which can be involved in their magnetic dynamics. Lanthanide (Ln) SMMs have provided some promising candidates since their discovery in 2003.[3,4] The design criteria to synthesise Ln SMMs,[5] with a single Dy^{III} centre in a highly axial ligand field environment to generate large magnetic anisotropy and to stabilise the highest $m_J = \pm 15/2$ spin state of Dy^{III} as the ground state, has led to Ln SMMs with magnetisation dynamics dominated by an Orbach-like (thermally activated) relaxation process, with very high values of the activation energy (Δ).[6–10] Two of the recent high-performing SMMs, $[Dy(OtBu)_2(py)_5][BPh_4]$ (**4**)[6a] and $[Dy(Cp^{ttt})_2][B(C_6F_5)_4]$ (**5**, Cp^{ttt}, $C_5H_2tBu_3$-1,2,4)[7] have similar Δ values (1815 K and 1760 K, respectively) but very different T_B^{100s} (12 K in **4** and 53 K in **5**; here we use T_B^{100s} to define the temperature at which the magnetic relaxation time is 100 s in zero field). The reasons behind the significant difference in T_B^{100s}, despite having comparable energy barriers, can be attributed to the differences in the other relaxation processes involved, for example, Raman and quantum tunnelling of magnetization (QTM), and therefore it is necessary to understand these mechanisms in detail to design higher-performing SMMs.[11–16] Therefore, systematic studies on a series of compounds from a given family are essential. In particular, a series of complexes with fine control of only one structural characteristic should be ideal to see its influence on their dynamic properties. To this point, only two large families of Dy-based SMMs with Δ/k_B > 1000 K are known: the pentagonal bipyramidal $[Dy(Solv)_5(L^1)(L^2)]$ (Solv = THF, Py; L^1 = O*t*Bu, Cl, Br, PhO; L^2 = O*t*Bu, Cl, Br, PhO) complexes[6] and the metallocene $[Dy(Cp^{R1})(Cp^{R2})]^+$ cations (R^1 = H, Me, *t*Bu, *i*Pr; R^2 = H, Me, *t*Bu, *i*Pr).[7–10]

Here we present a family of five-coordinate Dy SMMs, $[Dy(Mes^*O)_2(THF)_2X]$ (Mes^* = 2,4,6-tri-tert-butylphenyl) (X = Cl, **1**; Br, **2**; I, **3**), designed such that the Dy coordination sphere can be selectively varied at a single position to study its influence on the relaxation dynamics. In this system, the sterically demanding aryloxide ligand was employed to reduce the coordination number at the Dy centre. Alkoxide and aryloxide-based ligands have been widely used in Ln chemistry,[17] and in synthesising Ln SMMs in recent years.[6,14,18–20] The $[Dy(Mes^*O)_2(THF)_2X]$ complexes were prepared directly by the salt metathesis reactions of two equivalents of NaOMes* with the parent halide in THF (Scheme 1). Similarly, the diamagnetic Y(III) analogous compound, **1-Y** and a 5% doped sample **5%Dy@1-Y** were synthesised to perform complementary NMR spectroscopy and dilution experiments, respectively.

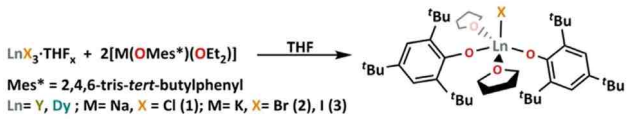

Scheme 1. Synthesis of **1**–**3**, **1-Y**, **2-Y** and **3-Y**.

[a] *V. S. Parmar, Dr. F. Ortu, Dr. N. F. Chilton, Dr. D. P. Mills, Prof. Dr. R. E. P. Winpenny*
Department of Chemistry, The University of Manchester
Oxford Road, Manchester, M13 9PL (UK)
E-mail: David.mills@manchester.ac.uk
Richard.Winpenny@manchester.ac.uk

[b] *Dr. X. Ma, Dr. R. Clérac*
CNRS, Centre de Recherche Paul Pascal
Univ. Bordeaux, CRPP, UMR 5031
33600 Pessac (France)
E-mail: rodolphe.clerac@crpp.cnrs.fr

The single-crystal X-ray analysis of **1**–**3** and **1-Y** (Figure 1 and Figures S1–S3 in Supporting Information) reveal that **1**, **2** and **1-Y** crystallise in the $P2_1/c$ space group, whereas **3** crystallises in C_2/c (Tables S1–S2). All molecules contain a Ln^{III} ion in a rare pentacoordinate distorted square-based pyramidal geometry,

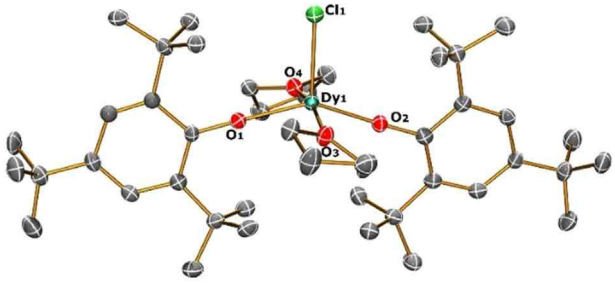

Figure 1. View of the $[Dy(OMes^*)_2(THF)_2Cl]$ molecular structure in **1** from its X-ray crystal structure at 100 K with thermal ellipsoids drawn at 50% probability level (Dy turquoise, Cl green, O red, C grey). H atoms are omitted for clarity.

having a halide anion at the apex of the pyramid with two *trans*-Mes*O ligands, and two *trans*-THF molecules making the square base (Tables S3–S4). The only monomeric five-coordinate Dy SMM known in the literature, $[Dy(NHAr)_3(THF)_2]$ (Ar = $C_6H_3iPr_2$-2,6),[21] has an energy barrier of 34 K, arising from a trigonal bipyramidal geometry with three anionic anilide donors and two neutral THF donors. The distortion of the coordination sphere for five-coordinate systems can be quantified by the geometric parameter $\tau_5 = (\beta - \alpha)/60$, where β and α are the largest and second-largest angles in the coordination sphere, respectively. The τ_5 parameter quantifies the degree of trigonality within the structural continuum between square-based pyramid ($\tau_5 = 0$) and trigonal bipyramid ($\tau_5 = 1$).[22] For complexes **1** to **3**, τ_5 was found to be 0.348, 0.344 and 0.340, respectively, which is consistent with a significantly distorted square-based pyramid (Table S4). This distortion is mainly due to the four O-donors in the square base, which are not in a single plane. In **1**, the angle at Dy between the O-donors from the THF ligand is 167.3(1)°, and the angle between the O-donors from aryloxide is 146.4(1)°. Continuous shape measurement calculations also favour a square-based pyramid (Table S5).[23]

The Dy–O bond distances for **1** to **3** (Table S3) for the anionic oxides O1 and O2 fall in the range 2.116(4) to 2.124(3) Å, whilst the neutral oxygen donors O3 and O4 show longer Dy–O bonds: for **1**, 2.370(3) and 2.352(3) Å; for **2**, 2.346(4) and 2.370(4) Å; for **3**, 2.366(3) and 2.366(3) Å. When moving from X = Cl to Br to I in the series, the Dy–X bond distance increases from 2.537(1) to 2.6981(6) to 2.9540(6) Å, which is attributed to the increase in the ionic radii of the halide present. The intermolecular nearest Dy··Dy distances in the crystal packing (Figures S4–S12) varies as 7.7, 7.9 and 10.7 Å for **1**, **2** and **3** respectively. Complex **1-Y** is isostructural to **1** (Tables S2–S4) with Y–Cl, Y–O1, Y–O2, Y–O3, Y–O4 distances and ∠(O1-Y-O2) angle being 2.529(2), 2.115(4), 2.111(4), 2.358(5), 2.327(4) Å and 145.1(2)°, respectively.

Ab initio complete active space self-consistent field spin-orbit (CASSCF-SO) calculations were performed on the crystal structures of **1**–**3** to gain further insight into their electronic structures. The calculations confirm that the *trans*-Mes*O ligand pair dominates the electronic structure and bestows strong magneto-crystalline anisotropy on the Dy^{III} ions; the calculated magnetic axis passes through the *trans*-Mes*O ligand pair and perpendicular to the halide (Figures S24–S26). The highest magnetic ground state $m_J = \pm 15/2$ (>97%; Table S6) of the $^6H_{15/2}$ multiplet is stabilised by the axial ligand field, where the energies of the first two excited states are for **1**: 596.1 and 997.7 K, for **2**: 630.6 and 1040.0 K and for **3**: 644.7 and 1063.4 K; the first excited state is well-described as $m_J = \pm 13/2$ (>95%), the second is dominated by $m_J = \pm 11/2$ (>80%), but the third and all subsequent states are highly mixed (Tables S6–S9). Analysis of the transition probabilities by utilising the average matrix elements of the Cartesian magnetic moment operators between electronic states suggests the thermal relaxation to be most likely via the third excited state with an activation energy of 1099.1, 1150.9 and 1178.6 K for the Cl, Br and I analogues, respectively, (Figure 2 and Figure S23).

To investigate the magnetic properties of this family of complexes, dc (direct current) and ac (alternating current) susceptibility measurements were performed. The temperature dependence of the dc magnetic susceptibility was performed under an applied field of 0.1 T (Figure S28). At 270 K, the measured χT values of 13.8, 13.7, 13.5 and 13.7 $cm^3 mol^{-1} K$, for **1**, **2**, **3** and **5%Dy@1-Y** (when normalised per mol of Dy complex) respectively, are close to the expected value (14.17 $cm^3 mol^{-1} K$) for a free Dy^{III} ion.[24] The continuous decrease of the χT product upon cooling to low temperatures suggests strong crystal-field splitting. The field dependence of magnetisation measured at multiple temperatures below 15 K (between ±7 T) shows slow magnetisation dynamics and blocking (Figures S29–32). The magnetisation at 1.85(1) K and 7 T saturates at $M_{sat} = 5.3$, 5.0, 4.6 and 5.3 $N_A\mu_B$ for **1**, **2**, **3** and **5%Dy@1-Y** (when normalised per mol of Dy complex), respectively. The slow dynamics observed by dc measurements were further studied using ac susceptibility with frequencies up to 10 kHz. As shown in Figures S33–40, the in-phase (χ') and out-of-phase (χ'') components of the ac susceptibility are strongly temperature and frequency dependent in zero-dc field for all the complexes. The magnetisation relaxation time and its associated distribution were estimated as a function of the temperature (Figure 3) from the fitting of the experimental χ' versus. ν and χ'' versus ν data to the generalised Debye model (see Figures S33–40).[25–27]

In zero dc-field, paramagnetic relaxation[26–28] usually involves the three main mechanisms including Raman, [28,29] thermally activated (Orbach-like)[28,30] and quantum tunnelling (QTM)[28] relaxation pathways, as summarised in the following equations [Eq. (1)and (2)]:

$$\tau^{-1} = \tau_{Raman}^{-1} + \tau_{Orbach}^{-1} + \tau_{QTM}^{-1} \quad (1)$$

$$\tau^{-1} = CT^n + \tau_0^{-1}\exp\left(-\frac{\Delta}{k_B T}\right) + \tau_{QTM}^{-1} \quad (2)$$

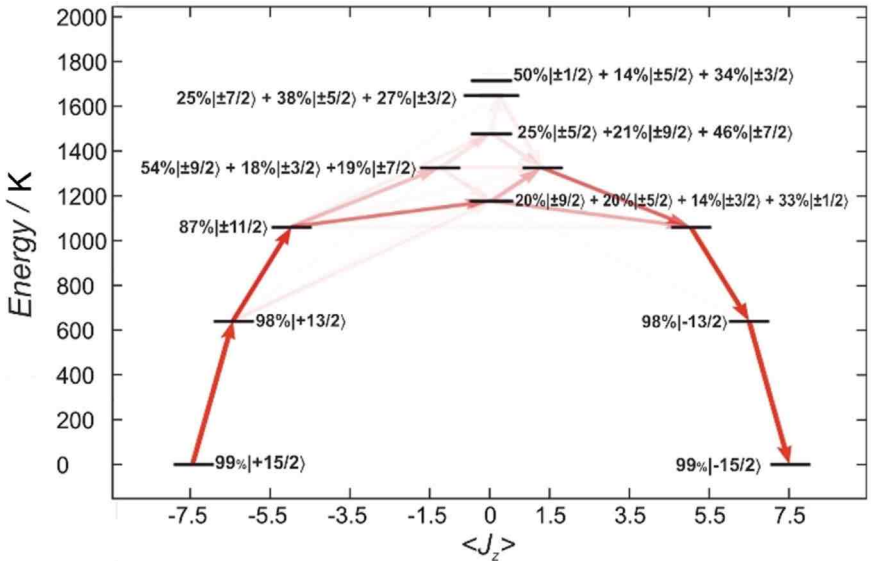

Figure 2. CASSCF-SO-calculated energy diagram of the ground-state multiplet for **1** indicating the zero-field magnetic transition propensities obtained from the average of the three Cartesian transition magnetic moment operators. The opacity of each arrow is proportional to the normalised transition propensity. The percentages of mixing have been rounded off to whole numbers and the contributions lower than 10% have been omitted for clarity.

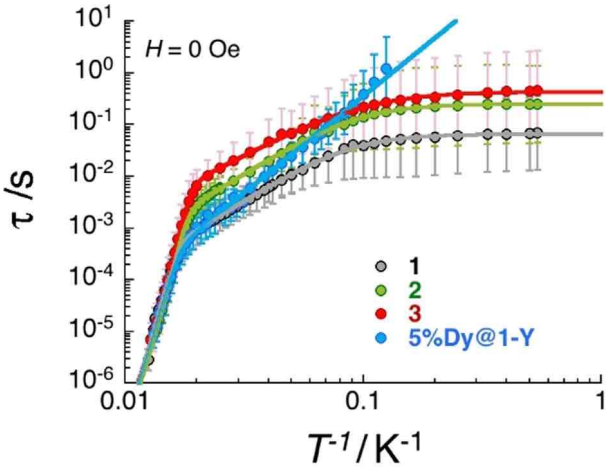

Figure 3. Temperature dependence of the relaxation time for **1**–**3** and **5%Dy@1-Y** estimated from the generalised Debye fits of the ac susceptibility data shown in Figures S33, S35, S37 and S39 collected under a zero applied field. The estimated standard deviations of the relaxation time (vertical solid bars) have been calculated from the α parameters of the generalised Debye fit (Figures S34, S36, S38 and S40) and the log-normal distribution as described in reference [27]. The solid lines are the best fit discussed in the text.

As shown in Figure 3, the above five-parameters model can reproduce almost perfectly the τ versus T^{-1} data for **1**, **2** and **3** (see Table 1), which clearly display three temperature domains associated with dominating Orbach (above ~55 K), Raman (~55–10 K) and QTM (below ~10 K) processes. It is interesting to note that the blocking temperature of these systems, T_B^{100s}, is not defined for **1**, **2** and **3,** as the QTM relaxation time is systematically smaller than 100 seconds. For the diluted compound, **5%Dy@1-Y**, the QTM regime is not observed in the available experimental window and thus the relaxation time was modelled considering only Orbach and Raman processes down to 8 K.

The first conclusion that can be drawn from these experimental results (Table 1), is that the activation energy of the Orbach process is statistically the same regardless of the halide present at $\Delta/k_B \approx 1200$ K, and does not change for **1** upon dilution; this result agrees with our CASSCF-SO calculations. The lack of change in Δ/k_B is probably because the halide is not on the principal anisotropy axis. The modification of the phonon bath moving from **1** to **5%Dy@1-Y** also has little influence on Δ/k_B. This conclusion is not surprising as the Orbach mechanism is primarily intrinsic to the electronic structure of the SMM, which is not much perturbed by the choice of halide here.

On the other hand, the halide substitution has a clear impact on the Raman relaxation with a characteristic time that increases as Cl < Br < I (Figure 3, Table 1). While the *C* and *n* parameters are relatively similar along the series, the intrinsic Raman relaxation time for a given temperature between 55 and 10 K (for example at 30 K which we define as τ_{Raman}^{30K}) changes by a factor of 8 between **1** and **3**. In contrast to the Orbach process, dilution significantly impacts the *C* and *n* parameters which decrease (/24) and increase (×1.3), respectively. This is a striking difference to the *bis*-cyclopentadienyl dysprosium(III) SMMs,[7] or in some pentagonal bipyramidal Dy SMMs, where there was no difference between the Raman parameters for the pure and doped materials.[6c] This suggests that **1** is far more sensitive to the precise crystal lattice and associated phonon bath. It is tempting to link this sensitivity to the faster relaxation observed here.

The halide variation also varies the QTM time which increases Cl < Br < I (by a factor 6 between the Cl and I analogues;

Table 1. Δ, τ_0, C, n and τ_{QTM} parameters generated from the fit of the relaxation time-temperature dependence (Figure 3) for **1**–**3** and **5%Dy@1-Y.** These parameters are given with their fitting error in parenthesis and their estimated standard deviations (±) based on the estimated standard deviations of the relaxation times shown in Figure 3.

Complex	**1**	**2**	**3**	**5%Dy@1-Y**
Δ/k_B [K]	1262(32) ± 199	1210(10) ± 91	1202(10) ± 174	1229(64) ± 260
a [$\tau_0 = 10^{-a}$ s]	12.2(2) ± 1.2	12.1(1) ± 0.6	11.9(1) ± 1.1	12.1(4) ± 1.6
c [$C = 10^{-c}$ s^{-1} K^{-n}]	1.9(1) ± 0.7	2.35(3) ± 0.82	2.1(1) ± 1.2	3.3(1) ± 0.4
N	2.9(1) ± 0.4	2.86(2) ± 0.51	2.42(4) ± 0.81	3.73(5) ± 0.25
b [$\tau_{QTM} = 10^{-b}$ s]	1.18(2) ± 0.25	0.59(1) ± 0.28	0.36(1) ± 0.31	$\gg$ 100
τ_{raman}^{30K} [10^{-2} s]	0.4	1.3	3.1	0.6

Table 1). However, this halide effect is relatively small when compared to the influence of the dilution as exemplified by at least a 20-fold enhancement of τ_{QTM} in **5%Dy@1-Y.** The large effect of dilution on the QTM time suggests that internal dipolar fields play a significant role in the efficiency of this mechanism. Hence, to determine if the differing QTM times for **1**–**3** arise from a simple change in the effective dipolar field, or due to something more intrinsic, we have performed classical simulations of the dipolar magnetic field in each compound. Taking the crystallographic coordinates of each compound, we simulate a classical magnetic dipole $S = 1/2$ with anisotropy given by the effective g-values from CASSCF-SO (Table S6), and perform stochastic spin flips under the field of all dipoles in a sphere of 40 Å radius. At the Dy^{III} ion at the centre of the sphere, we find the magnitude of the dipolar fields to be 20(7), 19(7), 15(8) and 4.8(6) Oe, for **1**, **2**, **3** and **5%Dy@1-Y**, respectively. Clearly the internal field for **5%Dy@1-Y** is far smaller than for the pure compounds, in agreement with the significantly reduced QTM. However, while there is a trend in the magnitude of the mean dipolar field for **1**–**3**, the standard deviations are significant such that these cannot be statistically distinguished. Hence, it is likely that another factor, potentially the mass or effective diffusion of charge of the halide, is also responsible for the change in the QTM time.

When considering the Dy-based SMMs listed in Table S11 together with this new series of five-coordinate Dy SMMs, it is relatively straightforward to draw conclusions about the key parameters that govern the different relaxation mechanisms. The first priority remains the design of the SMM to achieve the highest possible energy barrier of the Orbach relaxation. In that sense, the highest Δ/k_B, 2217(15) K, is found for $[Dy(C_5iPr_5)(C_5Me_5)][B(C_6F_5)_4]$ (**6**) that displays the highest T_B^{100s} (65 K).[8] But the literature shows that is very far from the only consideration. Indeed, **6** displays also the highest τ_{QTM} (25 000 s) and τ_{Raman}^{30K} (1195 s). Therefore, it is absolutely essential to increase simultaneously the characteristic time of the Raman and QTM processes in order to allow the Orbach mechanism to govern the magnetization relaxation over the largest possible temperature domain. The present study suggests that the use of heavier atoms within the ligand favours a significant slowing down of the Raman regime, and possibly also relaxation through QTM. Consequently, the use of more massive groups could be employed to enhance the performance further of already high-performing SMMs.

A more impressive step in this direction is found upon dilution, which does not affect Δ/k_B but does influence both Raman and QTM processes. This could be related to the utilization of bulky counter-anions (like $[B(C_6F_5)_4]^-$ or $[BPh_4]^-$) in the best performing SMMs listed in Table S11. Both dilution and the presence of large counter-anions seem to slow the non-Orbach processes. It is thus clear that the environment of the SMMs, needs to be controlled carefully in order to obtain high-performing SMMs.

Experimental

Full details of synthesis and characterisation of all materials can be found in the Supporting Information.

CCDC 1978052, 1978053, 1978054 and 1978055 contain the supplementary crystallographic data for this paper. These data are provided free of charge by The Cambridge Crystallographic Data Centre

Acknowledgements

V.P. thanks the University of Manchester for the President's Doctoral Scholarship. D.P.M. thanks the EPSRC (UK) for support (EP/P002560/1) and funding of a diffractometer (EP/P001386/1) and SQUID magnetometer. R.C. and X.M. thank the University of Bordeaux, the ANR, the CNRS, the Region Nouvelle Aquitaine, the MOLSPIN COST action CA15128, the GdR MCM-2: Magnétisme et Commutation Moléculaires and the Chinese Scholarship Council (CSC) for the PhD funding of X.M. R.E.P.W. thanks the ERC for an Advanced Grant (ERC-2017-ADG-786734) and EPSRC UK for an Established Career Fellowship (EP/R011079/1). N.F.C. thanks The Royal Society for a Research Fellowship. We acknowledge the University of Manchester for access to the Computational Shared Facility. Research data files supporting this publication are available from Mendeley Data at DOI:10.17632/jzgm7zjx7h.1.

[1] D. Gatteschi, R. Sessoli, J. Villain, *Molecular Nanomagnets*, Oxford University Press, Oxford, **2006**.

[2] M. N. Leuenberger, D. Loss, *Nature* **2001**, *410*, 789 – 793.

[3] N. Ishikawa, M. Sugita, T. Ishikawa, S. Y. Koshihara, Y. Kaizu, *J. Am. Chem. Soc.* **2003**, *125*, 8694 – 8695.

[4] K. L. M. Harriman, D. Errulat, M. Murugesu, *New Trends Chem. Teach.* **2019**, *1*, 425 – 439.

[5] J. D. Rinehart, J. R. Long, *Chem. Sci.* **2011**, *2*, 2078 – 2085.

[6] a) Y. S. Ding, N. F. Chilton, R. E. P. Winpenny, Y. Z. Zheng, *Angew. Chem. Int. Ed.* **2016**, *55*, 16071 – 16074; *Angew. Chem.* **2016**, *128*, 16305 – 16308; b) Y. S. Ding, K. X. Yu, D. Reta, F. Ortu, R. E. P. Winpenny, Y. Z. Zheng, N. F. Chilton, *Nature Commun.* **2018**, *9*, 3134; c) Y.-S. Ding, T. Han, Y.-Q. Zhai, D. Reta, N. F. Chilton, R. E. P. Winpenny, Y.-Z. Zheng, *Chem. Eur. J.* **2020**, *26*, 5893 – 5902.

[7] C. A. P. Goodwin, F. Ortu, D. Reta, N. F. Chilton, D. P. Mills, *Nature* **2017**, *548*, 439 – 442.

[8] F. S. Guo, B. M. Day, Y. C. Chen, M. L. Tong, A. Mansikkamäki, R. A. Layfield, *Science* **2018**, *362*, 1400 – 1403.

[9] K. R. McClain, C. A. Gould, K. Chakarawet, S. J. Teat, T. J. Groshens, J. R. Long, B. G. Harvey, *Chem. Sci.* **2018**, *9*, 8492 – 8503.

[10] P. Evans, D. Reta, G. F. S. Whitehead, N. F. Chilton, D. P. Mills, *J. Am. Chem. Soc.* **2019**, *141*, 19935 – 19940.

[11] A. Lunghi, S. Sanvito, *Sci. Adv.* **2019**, *5*, eaax7163.

[12] D. Gatteschi, R. Sessoli, *Angew. Chem. Int. Ed.* **2003**, *42*, 268 – 297; *Angew. Chem.* **2003**, *115*, 278 – 309.

[13] A. Lunghi, F. Totti, R. Sessoli, S. Sanvito, *Nat. Commun.* **2017**, *8*, 1 – 7.

[14] J. Liu, Y. C. Chen, J. L. Liu, V. Vieru, L. Ungur, J. H. Jia, L. F. Chibotaru, Y. Lan, W. Wernsdorfer, S. Gao, X. M. Chen, M. L. Tong, *J. Am. Chem. Soc.* **2016**, *138*, 5441 – 5450.

[15] J. L. Liu, Y. C. Chen, M. L. Tong, *Chem. Soc. Rev.* **2018**, *47*, 2431 – 2453.

[16] L. Escalera-Moreno, J. J. Baldoví, A. Gaita-Ariño, E. Coronado, *Chem. Sci.* **2018**, *9*, 3265 – 3275.

[17] T. J. Boyle, L. A. M. Ottley, *Chem. Rev.* **2008**, *108*, 1896 – 1917.

[18] R. J. Blagg, L. Ungur, F. Tuna, J. Speak, P. Comar, D. Collison, W. Wernsdorfer, E. J. L. McInnes, L. F. Chibotaru, R. E. P. Winpenny, *Nat. Chem.* **2013**, *5*, 673 – 678.

[19] Y. S. Meng, L. Xu, J. Xiong, Q. Yuan, T. Liu, B. W. Wang, S. Gao, *Angew. Chem. Int. Ed.* **2018**, *57*, 4673 – 4676; *Angew. Chem.* **2018**, *130*, 4763 – 4766.

[20] M. J. Giansiracusa, S. Al-Badran, A. K. Kostopoulos, G. F. S. Whitehead, D. Collison, F. Tuna, R. E. P. Winpenny, N. F. Chilton, *Dalton Trans.* **2019**, *48*, 10795 – 10798.

[21] P. Zhang, L. Zhang, C. Wang, S. Xue, S. Y. Lin, J. Tang, *J. Am. Chem. Soc.* **2014**, *136*, 4484 – 4487.

[22] A. W. Addison, T. N. Rao, J. Reedijk, J. Van Rijn, G. C. Verschoor, *J. Chem. Soc. Dalton Trans.* **1984**, 1349 – 1356.

[23] S. Alvarez, P. Alemany, D. Casanova, J. Cirera, M. Llunell, D. Avnir, *Coord. Chem. Rev.* **2005**, *249*, 1693 – 1708.

[24] O. Kahn, *Molecular Magnetism*, VCH, Weinheim, **1993**.

[25] K. S. Cole, R. H. Cole, *J. Chem. Phys.* **1941**, *9*, 341 – 351.

[26] A. Abragam, B. Bleaney, *Electron Paramagnetic Resonance of Transition Ions*, Clarendon Press. Oxford, **1970**.

[27] D. Reta, N. F. Chilton, *Phys. Chem. Chem. Phys.* **2019**, *21*, 23567 – 23575.

[28] K. N. Shrivastava, *Phys. Status Solidi* **1983**, *117*, 437 – 458.

[29] J. H. Van Vleck, *Phys. Rev.* **1940**, *57*, 426 – 447.

[30] R. Orbach, *Proc. R. Soc. London Ser. A* **1961**, *264*, 458 – 484.

Probing Relaxation Dynamics in Five-Coordinate Dysprosium Single-Molecule Magnets

Vijay S. Parmar,[a] Fabrizio Ortu,[a] Xiaozhou Ma,[b] Nicholas F. Chilton,[a] Rodolphe Clérac,*[b] David P. Mills,*[a] and Richard E. P. Winpenny*[a]

Contents

1. General experimental procedures

All syntheses and manipulations were conducted under argon with the rigorous exclusion of oxygen and water using Schlenk line and glovebox techniques. Diethylether and hexane were dried by refluxing over potassium and were stored over potassium mirrors. All solvents were degassed before use. For NMR spectroscopy C_6D_6 was dried by refluxing over potassium. NMR solvents were vacuum transferred and degassed by three freeze-pump-thaw cycles before use. Anhydrous $LnCl_3$ (Ln = Y or Dy) were purchased from Alfa Aesar and were used as received. ^1H (400 MHz) and $^{13}C\{^1H\}$ (100 MHz and 125 MHz), NMR spectra were obtained on an Avance III 400 MHz or 500 MHz spectrometers at 298 K. These were referenced to the solvent used, or to external TMS (^1H, ^{13}C). ATIR spectra were recorded as microcrystalline powders using a Bruker Tensor 27 ATR-Fourier Transform infrared (ATR-FTIR) spectrometer. Elemental analyses were performed by Mrs Anne Davies and Mr Martin Jennings at The University of Manchester, UK.

2. Experimental synthesis

$[Y(OMes^*)_2(THF)_2Cl]\cdot 3THF$ ***1-Y.*** YCl_3 (0.196 g; 1 mmol) was weighed in a Schlenk that was cooled to -78 ºC before adding 20 ml of THF. The reaction mixture was refluxed with continuous stirring for one hour to obtain the $YCl_3\cdot(THF)_x$ adduct. This adduct was then transferred to another Schlenk containing $NaOMes^*\cdot Et_2O$ (0.717 g; 2 mmol; see Figures S13-S14 for NMR) in 10 ml of THF. The resulting reaction mixture was stirred at room temperature for 16 hours. After the stirring was stopped, the cloudy reaction mixture settles into a white powder (NaCl) and clear, colourless supernatant (product). The colourless supernatant solution was filtered and concentrated to get colourless block-shaped crystals (0.590 g, 0.59 mmol; 59%) in about 36 hours at 0 ºC. The crystals were dried in vacuo to afford a white crystalline solid, which elemental analysis and ^1H NMR spectroscopy integrals indicate is partially desolvated **1-Y**, with 0.5 molecules of lattice THF remaining in the sample. Anal. Calcd for $C_{46}H_{78}ClO_{4.5}Y$: C, 66.77; H, 9.50. Found: C, 60.47; H, 9.38. Elemental analysis results show lower carbon values than predicted, which can be attributed to carbide formation from incomplete combustion. ^1H NMR (400.07 MHz, C_6D_6, 298 K, ppm): δ = 1.04, (m, 10H, THF), 1.41 (s, 18H, *p*-$C(CH_3)_3$), 1.74 (s, 36H, o-$C(CH_3)_3$), 3.76 (m, 10H, THF), 7.57 (s, 4H, *m*-CH) (see Figure S15(top)). $^{13}C\{^1H\}$ NMR (400.07 MHz, C_6D_6, 298 K, ppm): δ =

25.04 (s), 30.48 (s), 32.01 (s), 32.08 (s), 34.58 (s), 35.92 (s), 71.58, 122.10 (s), 137.74 (s), 138.09 (s) (see Figure S15(bottom)). FTIR (ATR, microcrystalline): ũ = 2955 (m, br), 2871 (w, br), 1458 (w), 1384 (w), 1358 (w), 1240 (s), 1201 (m), 1152 (w), 1119 (m), 1046 (m), 917 (w), 836 (s, br), 779 (w), 748 (m), 673 (w), 644 (w), 534 (m), 458 (m) cm^{-1} (see Figures S8, S9, S10 and S11).

[Dy(OMes)$_2$(THF)$_2$Cl]·3THF* ***1***. The synthetic procedure and crystallization employed for **1** are identical to that of **1-Y** using $DyCl_3$ (0.269 g; 1 mmol). Complex **1** was obtained as pale yellow coloured crystals (0.424 g, 0.39 mmol; 39%). The crystals were dried in vacuo to afford a white crystalline solid, which elemental analysis and NMR analysis of its Y analogue (**1-Y**) indicate is partially desolvated **1**, with half a molecules of lattice THF remaining in the sample. Anal. Calcd for $C_{48}H_{78}ClO_{4.5}Dy$: C, 61.31; H, 8.72. Found: C, 59.43; H, 8.83. Elemental analysis results show lower carbon values than predicted, which we attribute to carbide formation from incomplete combustion. μ_{eff} = 10.38 μ_B mol^{-1}, χT = 13.47 cm^3 mol^{-1} K (Evans method).[1,2] FTIR (ATR, microcrystalline): ũ = 2955 (m, br), 2904 (w, br), 1456 (w), 1384 (w), 1358 (w), 1231 (s), 1201 (m), 1152 (w), 1119 (m), 1011 (m), 921 (w), 832 (s, br), 781 (w), 746 (m), 673 (w), 642 (w), 530 (m), 452 (m) cm^{-1} (see Figures S16, S20, S21 and S22).

[Dy(OMes)$_2$(THF)$_2$Br]·3THF* ***2.*** A mixture of $DyBr_3$ (0.403 g; 1 mmol) and two equivalents of KOMes* (0.605 g; 2 mmol) weighed in a 100 ml Schlenk was cooled to -78ºC before adding 30ml of THF. The reaction mixture was warmed to 74ºC and refluxed with continuous stirring for 1.5 hours, then stirred at room temperature for further 16 hours. After the stirring was stopped, the cloudy reaction mixture settles into a grey powder (KBr) and clear, colourless supernatant (product). The supernatant was filtered out to a 20 mL Schlenk and concentrated further to get colourless block-shaped crystals (0.672 g, 0.59 mmol; 59%) when stored for 36 hours at 0ºC. The crystals were dried in vacuo to afford a white crystalline solid, which elemental analysis indicate is partially desolvated **2**, with one molecules of lattice THF remaining in the sample. Anal. Calcd for $C_{48}H_{82}BrO_5Dy$: C, 58.73; H, 8.42. Found: C, 58.86; H, 8.53. μ_{eff} = 10.40 μ_B mol^{-1}, χT = 13.52 cm^3 mol^{-1} K (Evans method).[1,2] FTIR (ATR, microcrystalline): ũ = 2955 (m, br), 2904 (w, br), 1456 (w), 1384 (w), 1358 (w), 1229 (s), 1201 (m), 1152 (w),

1117 (m), 1011 (m), 921 (w), 830 (s, br), 779 (w), 744 (m), 673 (w), 642 (w), 530 (m), 452 (m) cm^{-1} (see Figures S17, S20, S21 and S22).

[Dy(OMes)$_2$(THF)$_2$I]·2THF* ***3.*** The synthetic procedure and crystallization employed for **3** are identical to that of **2** using DyI_3 (0.544 g; 1 mmol). Complex **3** was obtained as colourless block-shaped crystals (0.355 g, 0.32 mmol; 32%). The crystals were dried in vacuo to afford a plale brown crystalline solid, which elemental analysis results indicate is **3**. Anal. Calcd for $C_{52}H_{90}IO_6Dy$: C, 56.74; H, 8.24. Found: C, 56.08; H, 8.25. μ_{eff} = 10.27 μ_B mol^{-1}, χT = 13.17 cm^3 mol^{-1} K (Evans method).[1,2] FTIR (ATR, microcrystalline): ũ = 2955 (m, br), 2904 (w, br), 1415 (w), 1384 (w), 1358 (w), 1227 (s), 1199 (m), 1154 (w), 1117 (m), 1013 (m), 919 (w), 830 (s, br), 779 (w), 744 (m), 671 (w), 642 (w), 530 (m), 452 (m) cm^{-1} (see Figures S18, S20, S21 and S22).

5%Dy@[Y(OMes)$_2$(THF)$_2$Cl]* **.** The synthetic procedure and crystallization employed here are identical to that of **1-Y** using $DyCl_3$ (0.013 g; 0.05 mmol) and YCl_3 (0.186 g; 0.95 mmol). The product was obtained as colourless block-shaped crystals (0.362 g, 0.46 mmol; 46%). Anal. Calcd for $C_{44}HClO_4Dy_{0.05}Y_{0.95}$: C, 66.47; H, 9.38. Found: C, 64.70; H, 9.56. Y/Dy composition (ICP-OES): Y, 94.8; Dy, 5.2.

3. Crystallography

The crystal data for complexes **1**, **2**, **3** and **1-Y** are compiled in Table S1 and Table S2. Crystals of **1**, and **3** were examined using an Oxford Diffraction Supernova diffractometer, equipped with CCD area detector and a mirror-monochromated Mo K_α radiation (λ = 0.71073 Å). Crystals of **2** were examined using an Oxford Diffraction Xcalibur diffractometer, equipped with CCD area detector and a mirror-monochromated Mo Kα radiation (λ = 0.71073 Å). Crystals of **1-Y** were examined using a Bruker Apex II diffractometer, equipped with CCD area detector and a graphite-monochromated Cu Kα radiation (λ = 1.54178 Å). Intensities were integrated from data recorded on 1° frames by ω rotation. Cell parameters were refined from the observed positions of all strong reflections in each data set. A multi-scan absorption correction with a beam profile was applied.[3] The structures were solved using direct methods by SHELXS; the datasets were refined by full-matrix least-squares on all unique F^2 values [4] CrysAlisPro [3] was used for control and integration, and SHELX[4,5] was employed through OLEX2[6] for structure solution and refinement. ORTEP-3[7] and POV-Ray[8] were employed for molecular graphics. CCDC 1978052-1978055 contain the supplementary crystal data for this article. These data can be obtained free of charge from the Cambridge Crystallographic Data Centre via www.ccdc.cam.ac.uk/data_request/cif. Single crystals of **5%Dy@1-Y** were screened in order to verify the doped sample was of the correct structure; these afforded cell parameters consistent with those of **1** and **1-Y**: a = 17.5646(8) Å, b = 15.9911(8) Å, c = 20.6806(7) Å, α = 90°, β = 102.270(4)°, γ = 90°, V = 5676.0(4) Å^3.

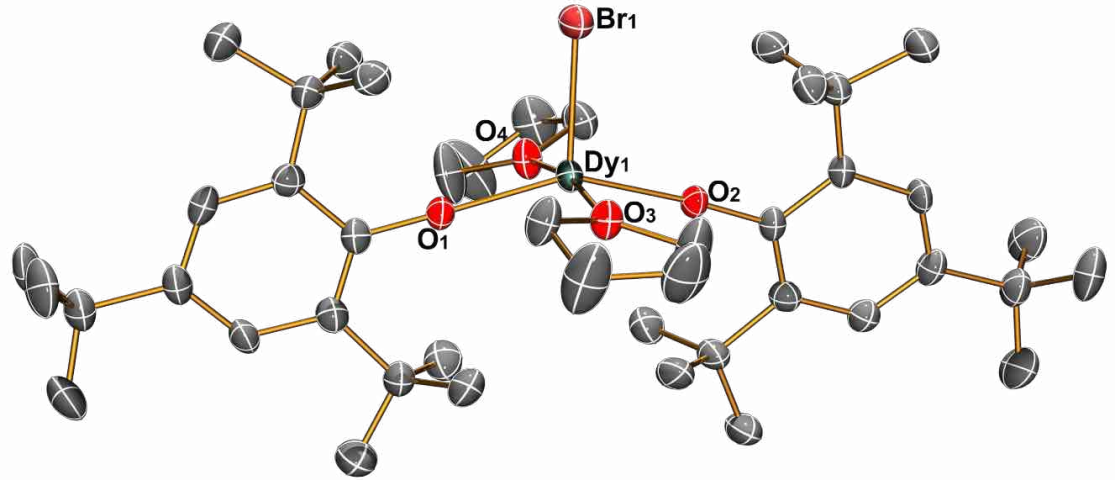

Figure S1: View of the [Dy(OMes*)$_2$(THF)$_2$Br] molecular structure in **2** from its X-ray crystal structure at 150 K with thermal ellipsoids drawn at 50% probability level (Dy turquoise, Br gold, O red, C grey). H atoms and lattice solvent are omitted for clarity.

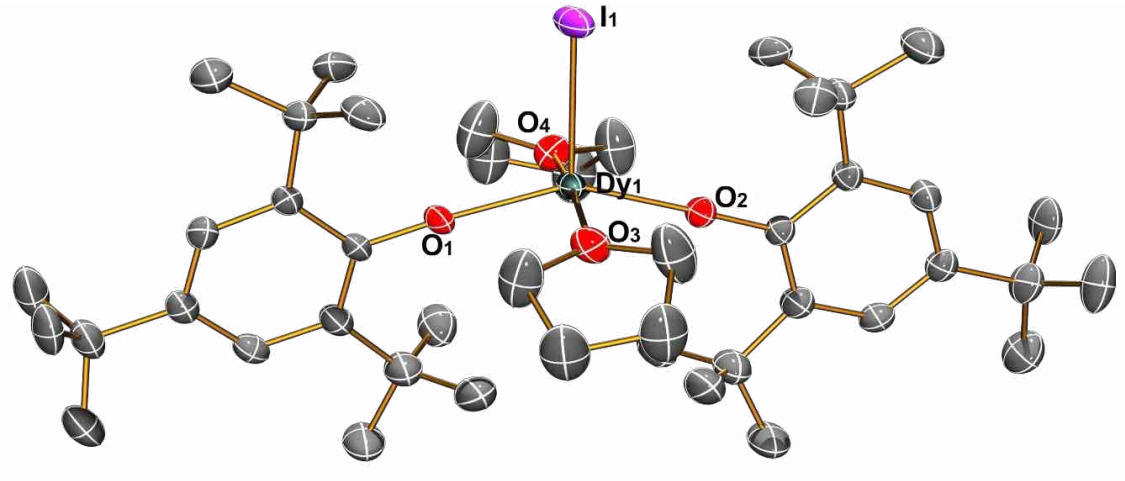

Figure S2: View of the [Dy(OMes*)$_2$(THF)$_2$I] molecular structure in **3** from its X-ray crystal structure at 150 K with thermal ellipsoids drawn at 50% probability level (Dy turquoise, Y purple, O red, C grey). H and lattice solvent atoms are omitted for clarity.

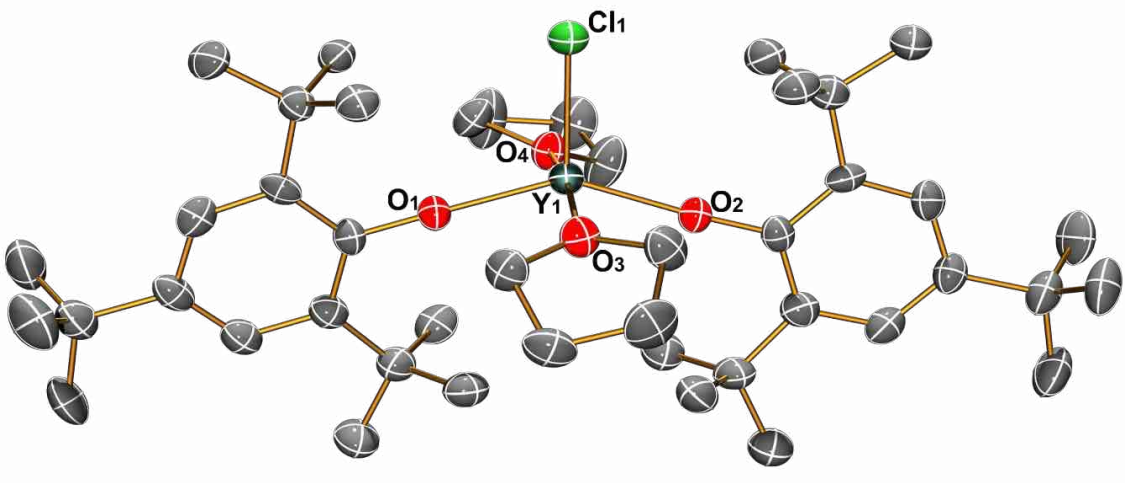

Figure S3: View of the [Y(OMes*)$_2$(THF)$_2$Cl] molecular structure in **1-Y** from its X-ray crystal structure at 150 K with thermal ellipsoids drawn at 50% probability level (Dy turquoise, Cl green, O red, C grey). H atoms and lattice solvent are omitted for clarity.

Table S1. Crystallographic data for **1**, **2** and **3.**

	1	**2**	**3**
Formula	$C_{56}H_{98}ClDyO_7$	$C_{56}H_{98}BrDyO_7$	$C_{52}H_{90}IDyO_6$
Fw	1081.33	1125.75	1100.63
Crystal size, mm	0.214 × 0.231 × 0.25	0.22 × 0.29 × 0.48	0.07 × 0.09 × 0.12
Temperature, K	100	150	150
Crystal system	monoclinic	monoclinic	monoclinic
Space group	$P2_1/c$	$P2_1/c$	$C2/c$
a, Å	18.2032(5)	17.6562(4)	18.7399(6)
b, Å	15.1042(5)	16.0269(3)	10.5463(4)
c, Å	20.7545(7)	20.7311(4)	27.7967(8)
α, °	90°	90°	90
β, °	99.431(3)°	102.230(2)°	94.770(3)
γ, °	90°	90°	90
V, Å^3	5629.2(3)	5733.2(2)	5474.6(3)
Z	4	4	4
ρ_{calcd}, g cm^3	1.276	1.304	1.335
μ, mm^{-1}	1.422	2.046	1.971
F(*000*)	2292	2364	2276
nb. of reflections (unique)	32566 (11493)	59086 (11714)	21465(6517)
nb. of parameters	576	696	377
S[a]	1.082	1.041	1.017
R_1 ($I > 2\sigma(I)$)	0.0504	0.0505	0.0449
wR_2 *all*	0.1242	0.1240	0.1138
R_{int}	0.0497	0.0698	0.0557
min./max. diff map, Å^{-3}	–1.145, 3.352	–0.998, 2.028	–1.367, 1.312

[a]Conventional $R = \Sigma||F_o| - |F_c||/\Sigma|F_o|$; $R_w = [\Sigma w(F_o^2 - F_c^2)^2/\Sigma w(F_o^2)^2]^{1/2}$; $S = [\Sigma w(F_o^2 - F_c^2)^2/\text{no. data} - \text{no. params})]^{1/2}$ for all data.

Table S2. Crystallographic data for **1** and **1-Y.**

	1	**1-Y**
Formula	$C_{56}H_{98}ClDyO_7$	$C_{56}H_{98}ClO_7Y$
Fw	1081.33	1007.70
Crystal size, mm	0.214 × 0.231 × 0.25	0.1 × 0.3 × 0.3
Temperature / K	100	150
Crystal system	monoclinic	monoclinic
Space group	$P2_1/c$	$P2_1/c$
a, Å	18.2032(5)	18.2094(5)
b, Å	15.1042(5)	15.2650(3)
c, Å	20.7545(7)	20.7616(5)
α, °	90°	90
β, °	99.431(3)°	99.492(3)
γ, °	90°	90
V, Å^3	5629.2(3)	5692.0(2)
Z	4	4
ρ_{calcd}, g cm^3	1.276	1.176
μ, mm^{-1}	1.422	2.232
F(*000*)	2292	2184
nb. of reflections (unique)	32566 (11493)	15778(15778)
nb. of parameters	576	661
S[a]	1.083	1.026
R_1 ($I > 2\sigma(I)$)	0.0504	0.0807
wR_2	0.1242	0.2119
R_{int}	0.0497	0.2704
min./max. diff map, Å^{-3}	–1.145, 3.352	–0.670, 1.020

[a]Conventional $R = \Sigma||F_o| - |F_c||/\Sigma|F_o|$; $R_w = [\Sigma w(F_o^2 - F_c^2)^2/\Sigma w(F_o^2)^2]^{1/2}$; $S = [\Sigma w(F_o^2 - F_c^2)^2/\text{no. data} - \text{no. params})]^{1/2}$ for all data.

Table S3: Selected bond lengths (Å) in complexes **1**, **2**, **3** and **1-Y.**

	1	**2**	**3**	**1-Y**
Ln-O1	2.124(3)	2.116(3)	2.124(3)	2.115(4)
Ln-O2	2.121(3)	2.120(3)	2.124(3)	2.111(4)
Ln-O3	2.370(3)	2.346(4)	2.366(3)	2.358(5)
Ln-O4	2.352(3)	2.370(4)	2.366(3)	2.327(4)
Ln-X	2.537(1)	2.6981(6)	2.9540(6)	2.529(2)

Table S4: Selected bond angles (°) in complexes **1**, **2**, **3** and **1-Y.**

	1	**2**	**3**	**1-Y**
O1-Ln-O2	146.4(1)	148.3(1)	148.3(2)	145.1(2)
O1-Ln-O3	86.6(1)	88.3(1)	88.0(1)	87.1(2)
O1-Ln-O4	91.8(1)	86.1(1)	88.0(1)	90.7(2)
O2-Ln-O3	85.8(1)	90.9(1)	88.9(1)	86.1(2)
O2-Ln-O4	88.6(1)	88.9(1)	88.9(1)	88.8(2)
O3-Ln-O4	167.3(1)	168.9(1)	168.8(1)	167.8(2)
X-Ln-O1	108.82(9)	108.0(1)	105.85(9)	109.3(1)
X-Ln-O2	104.35(9)	103.4(1)	105.85(9)	105.5(1)
X-Ln-O3	94.53(8)	98.43(9)	95.61(8)	95.0(1)
X-Ln-O4	97.95(8)	92.4(1)	95.61(8)	97.0(1)

Table S5: Continuous Shape Measures (**CShM**)[9] calculations for complexes **1-3**.

	Structure[a]	PP-5	vOC-5	TBPY-5	SPY-5	JTBPY-5
1	**CShM**	33.641	2.700	2.599	1.012	4.550
2	**CShM**	32.722	3.075	2.729	1.194	5.028
3	**CShM**	35.235	4.035	3.092	1.539	5.967

[a] PP-5 Pentagon (D_{5h})

vOC-5 Vacant octahedron (C_{4v})

TBPY-5 Trigonal bipyramid (D_{3h})

SPY-5 Spherical square pyramid (C_{4v})

JTBPY-5 Johnson trigonal bipyramid J12 (D_{3h})

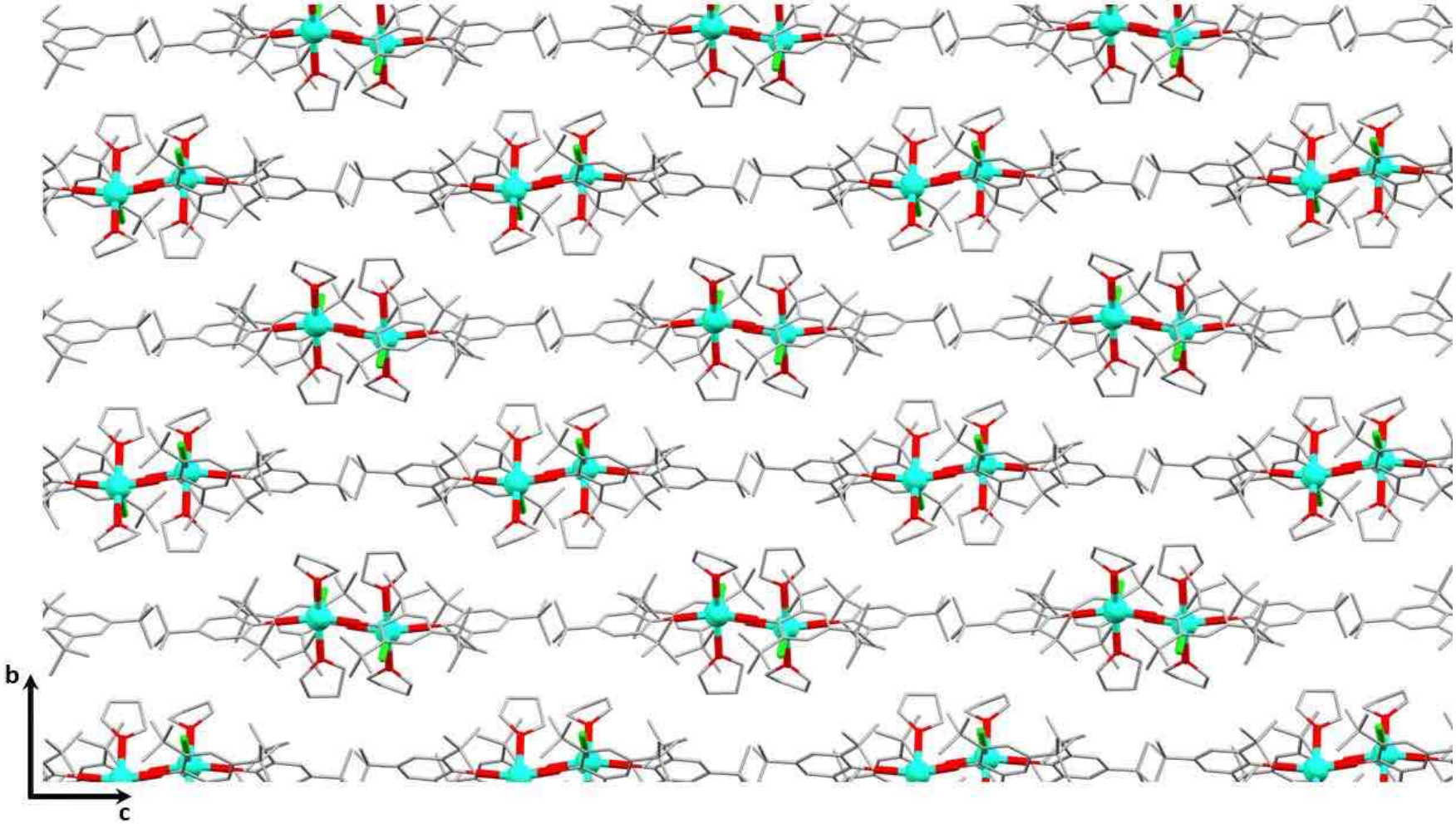

Figure S4: View of the crystal packing in [Dy(OMes*)$_2$(THF)$_2$Cl] **1** along the x-axis (Dy turquoise, I purple, O red, C grey). H atoms and lattice solvent are omitted for clarity.

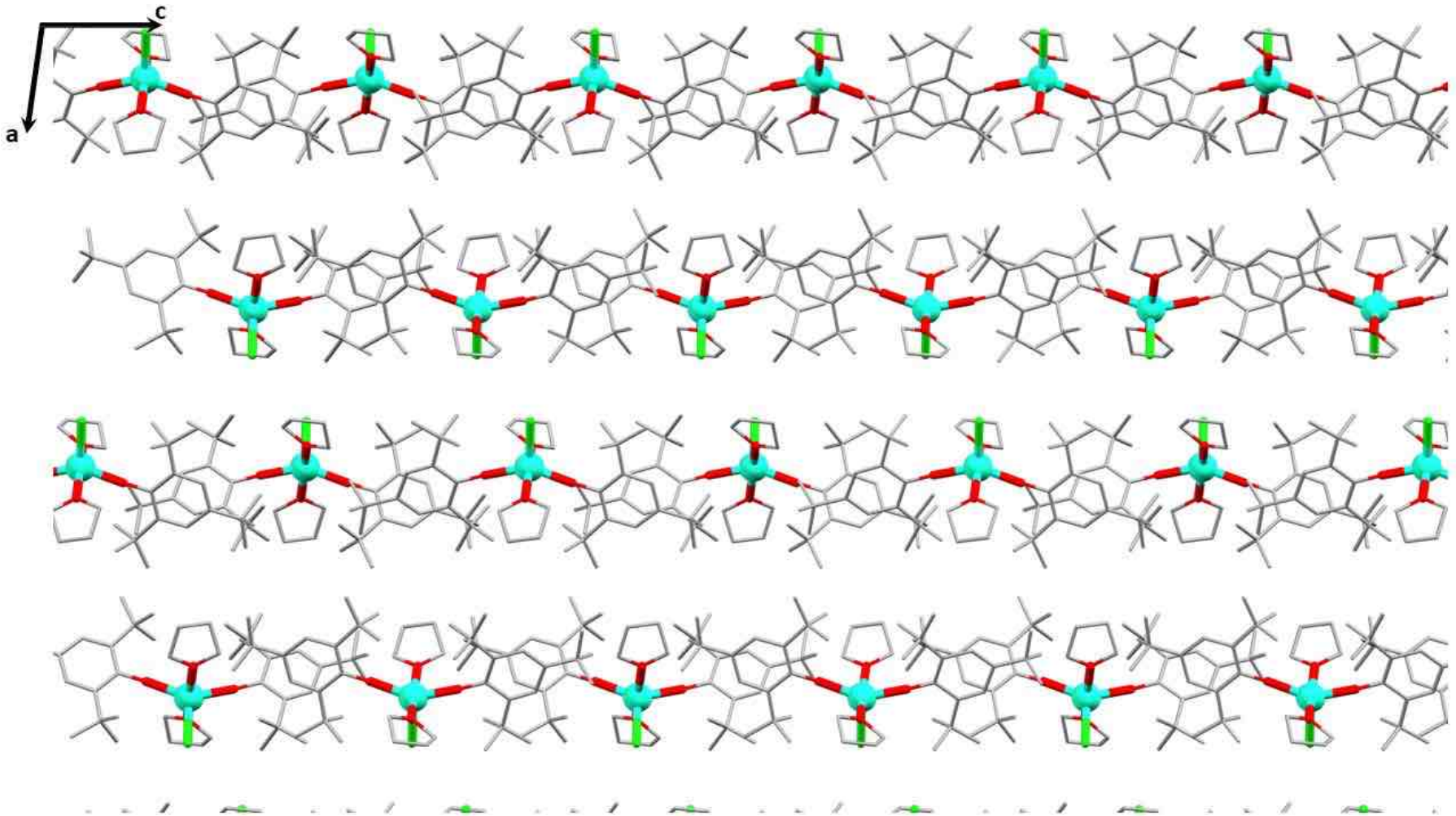

Figure S5: View of the crystal packing in [Dy(OMes*)$_2$(THF)$_2$Cl] **1** along the y-axis (Dy turquoise, I purple, O red, C grey). H atoms and lattice solvent are omitted for clarity.

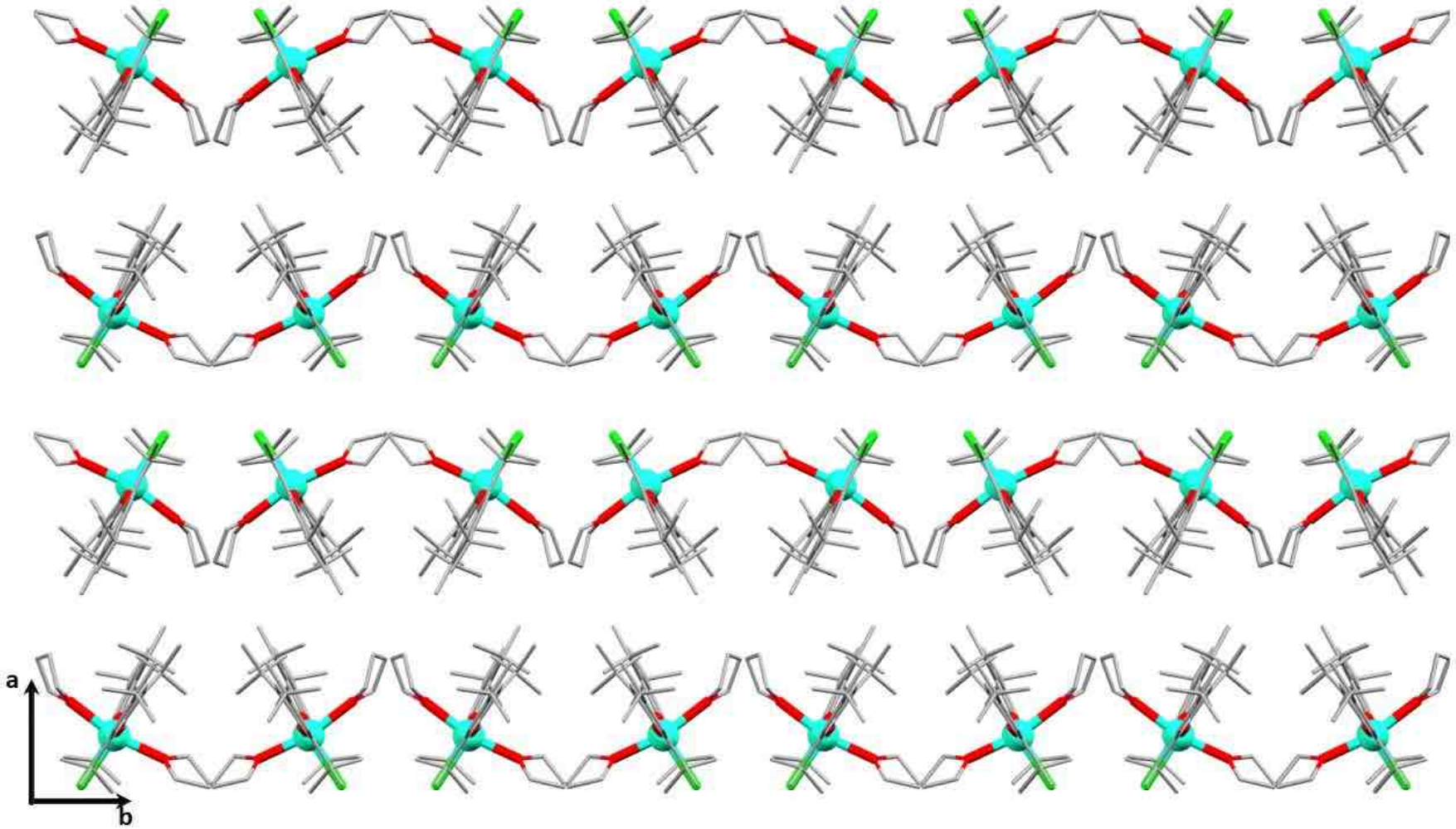

Figure S6: View of the crystal packing in [Dy(OMes*)$_2$(THF)$_2$Cl] **1** along the z-axis (Dy turquoise, I purple, O red, C grey). H atoms and lattice solvent are omitted for clarity.

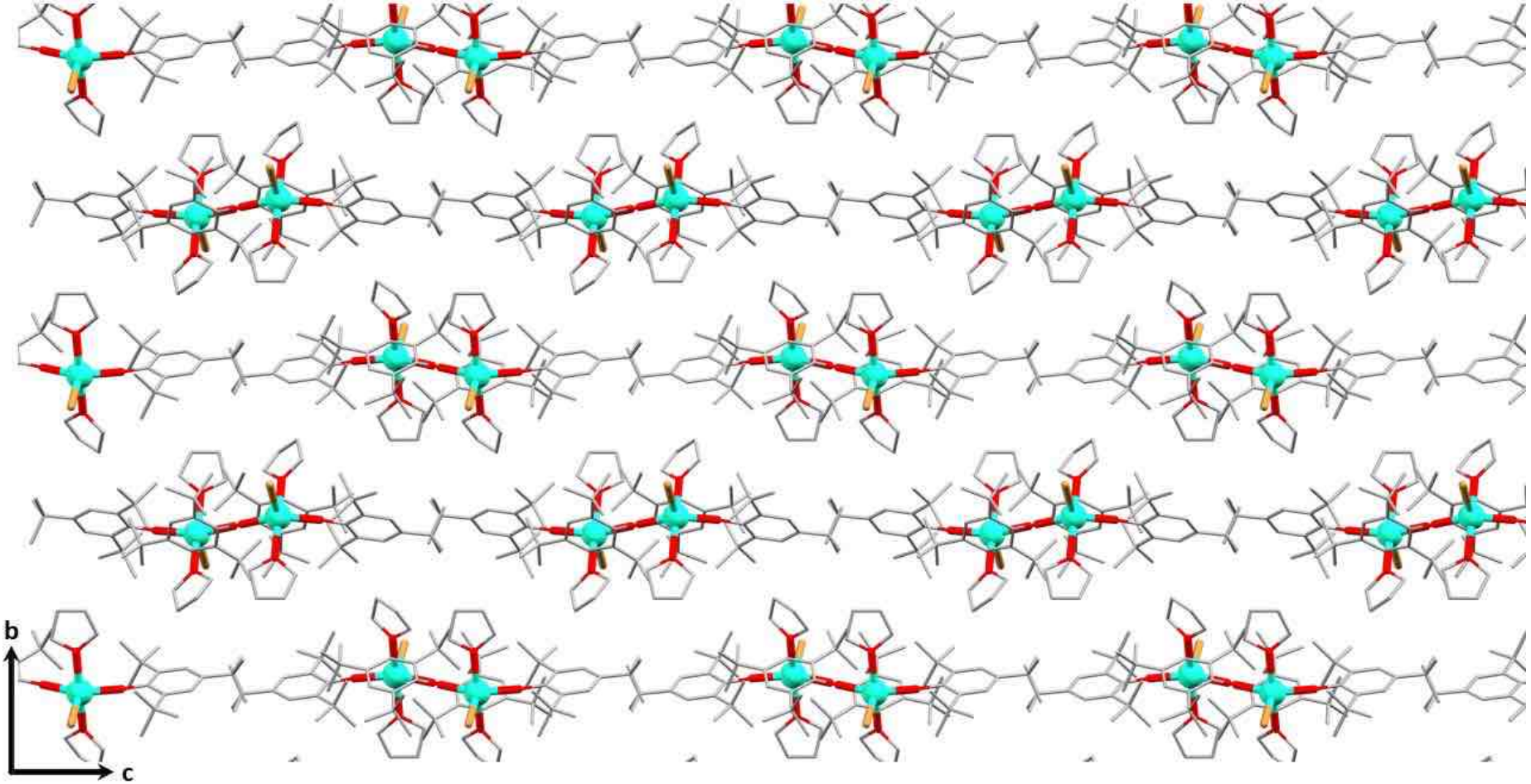

Figure S7: View of the crystal packing in [Dy(OMes*)$_2$(THF)$_2$Br] **2** along the x-axis (Dy turquoise, I purple, O red, C grey). H atoms and lattice solvent are omitted for clarity.

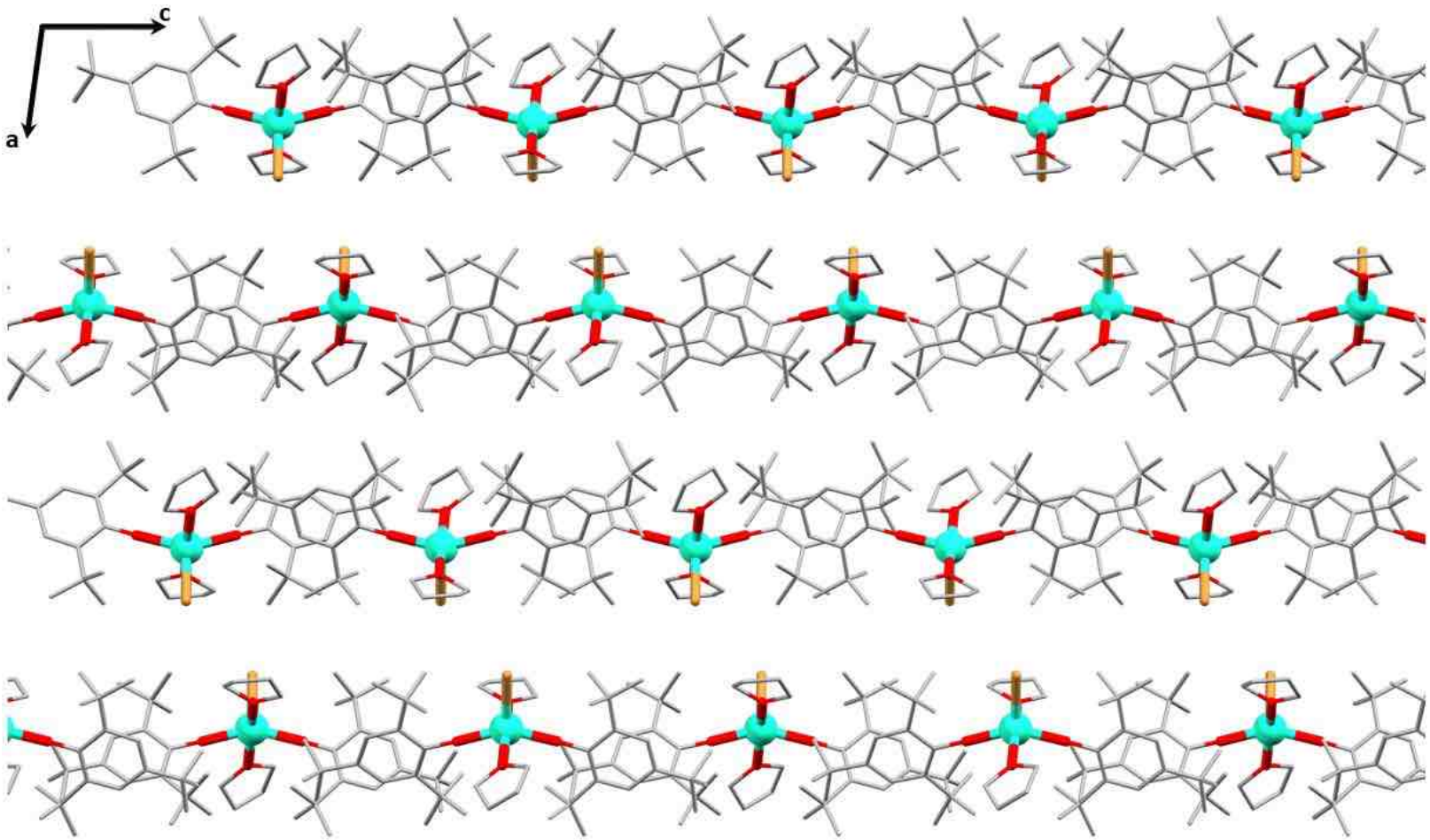

Figure S8: View of the crystal packing in [Dy(OMes*)$_2$(THF)$_2$Br] **2** along the y-axis (Dy turquoise, I purple, O red, C grey). H atoms and lattice solvent are omitted for clarity.

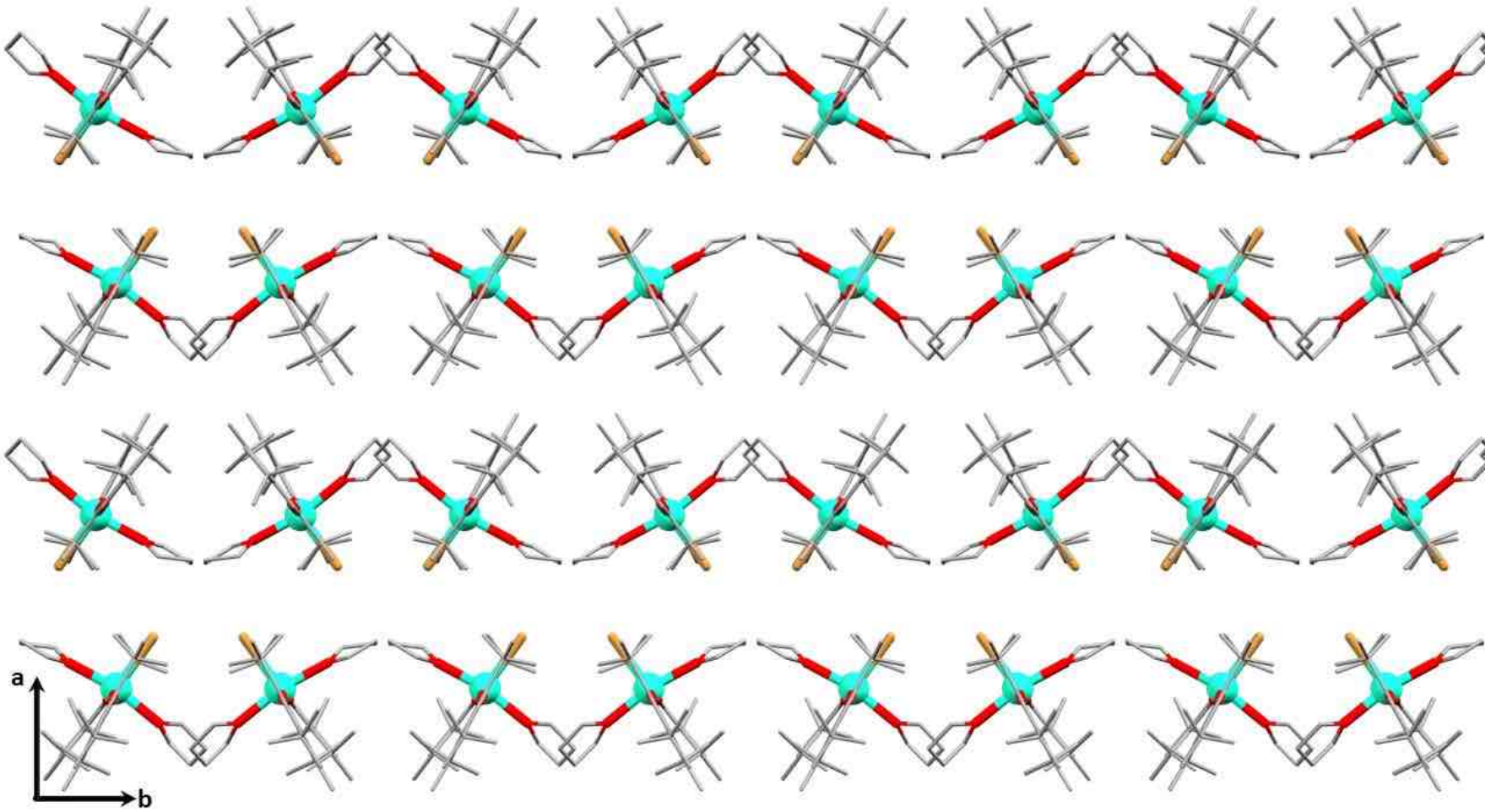

Figure S9: View of the crystal packing in [Dy(OMes*)$_2$(THF)$_2$Br] **2** along the z-axis (Dy turquoise, I purple, O red, C grey). H atoms and lattice solvent are omitted for clarity.

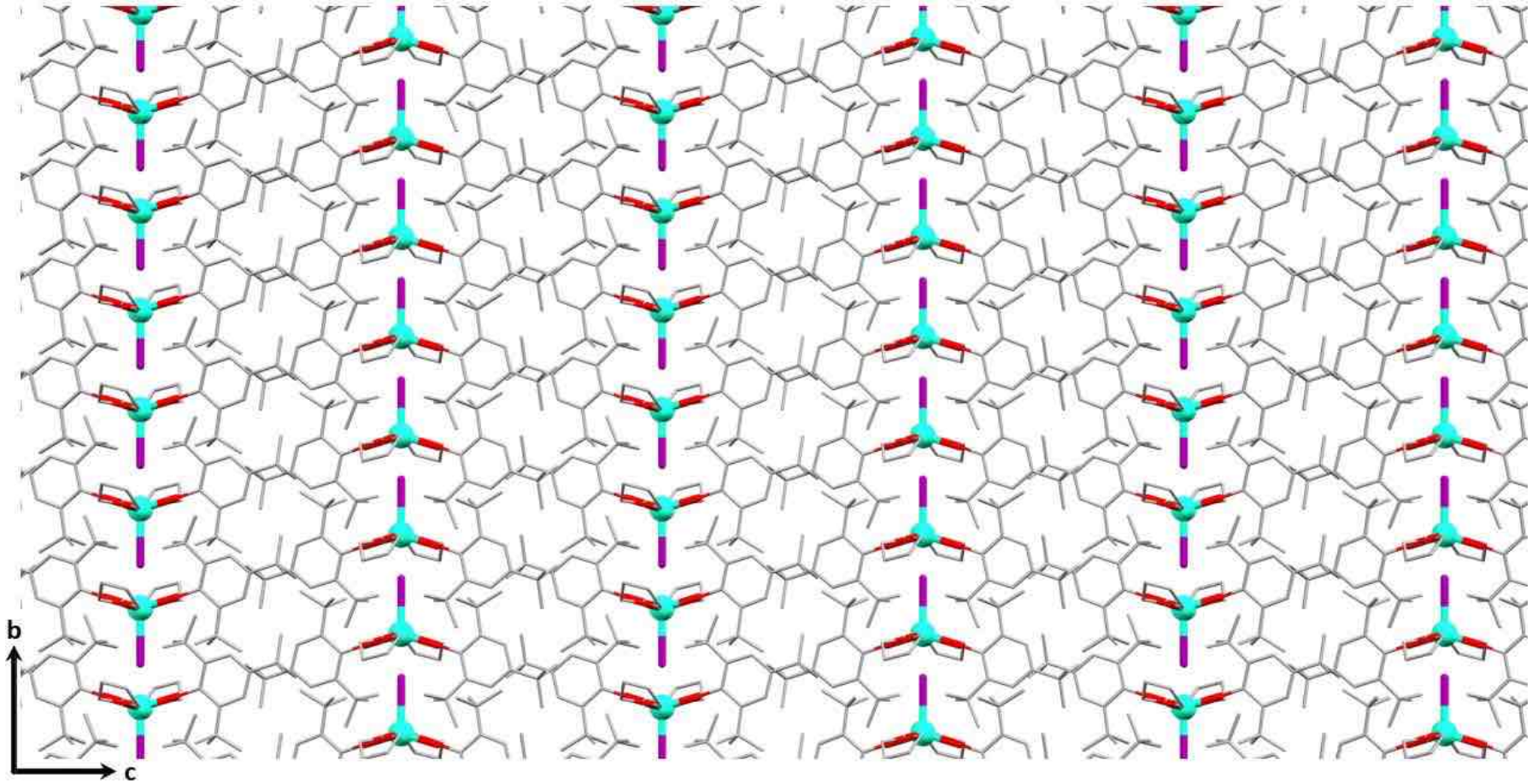

Figure S10: View of the crystal packing in [Dy(OMes*)$_2$(THF)$_2$I] **3** along the x-axis (Dy turquoise, I purple, O red, C grey). H atoms and lattice solvent are omitted for clarity.

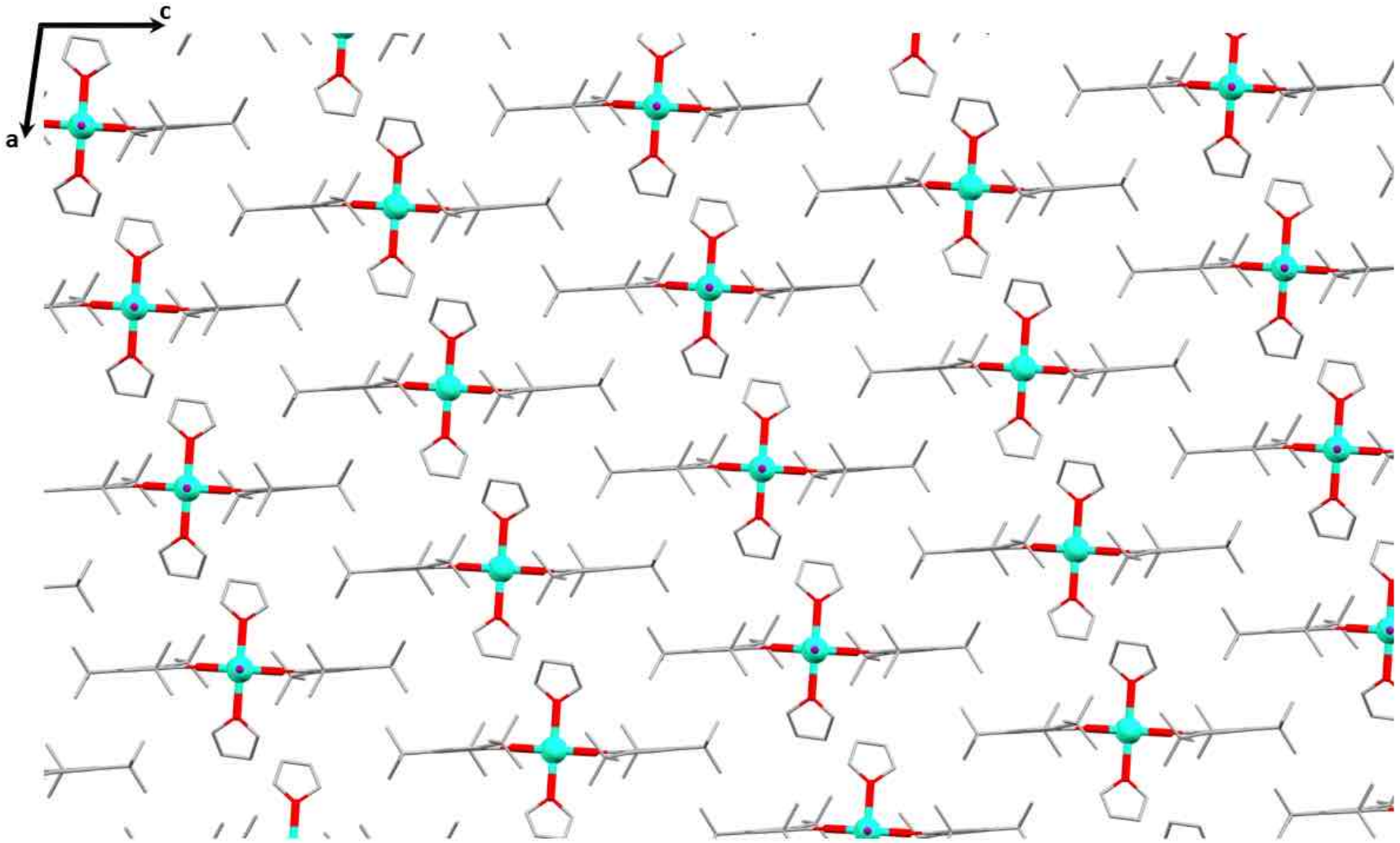

Figure S11: View of the crystal packing in [Dy(OMes*)$_2$(THF)$_2$I] **3** along the y-axis (Dy turquoise, I purple, O red, C grey). H atoms and lattice solvent are omitted for clarity.

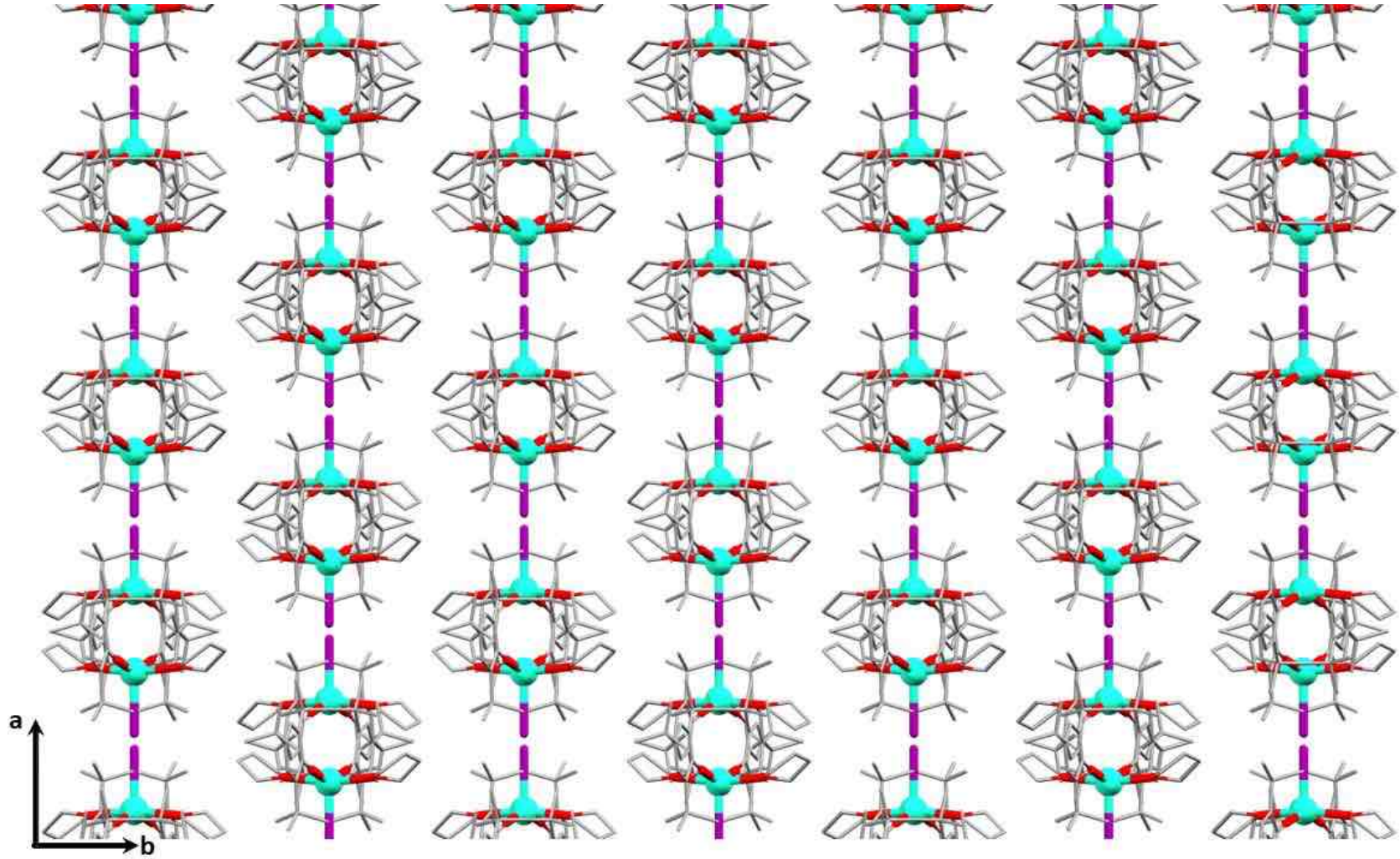

Figure S12: View of the crystal packing in [Dy(OMes*)$_2$(THF)$_2$I] **3** along the z-axis (Dy turquoise, I purple, O red, C grey). H atoms and lattice solvent are omitted for clarity.

4. NMR spectra

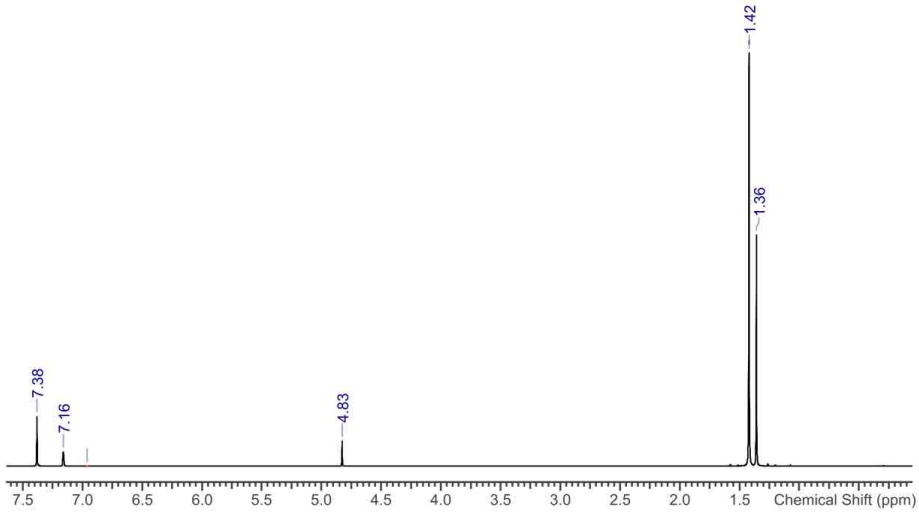

Figure S13. ^{1}H NMR spectrum of ligand precursor Mes*OH (2,4,6-tri-*tert*-butylphenol) in benzene (solvent reference peak: 7.16).

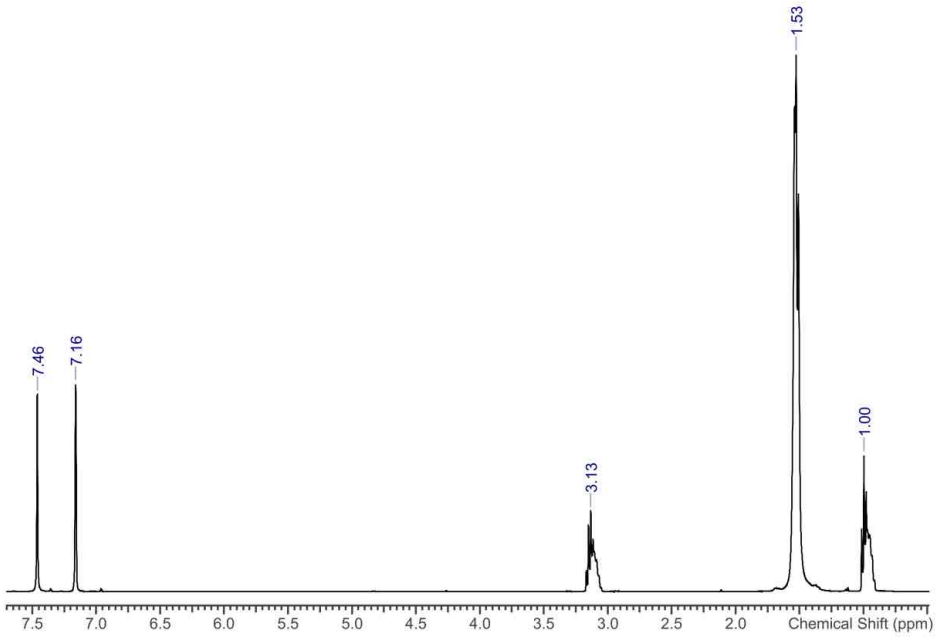

Figure S14. ^{1}H NMR spectrum of group 1 transfer agent Mes*ONa·Et_2O in benzene (solvent reference peak: 7.16).

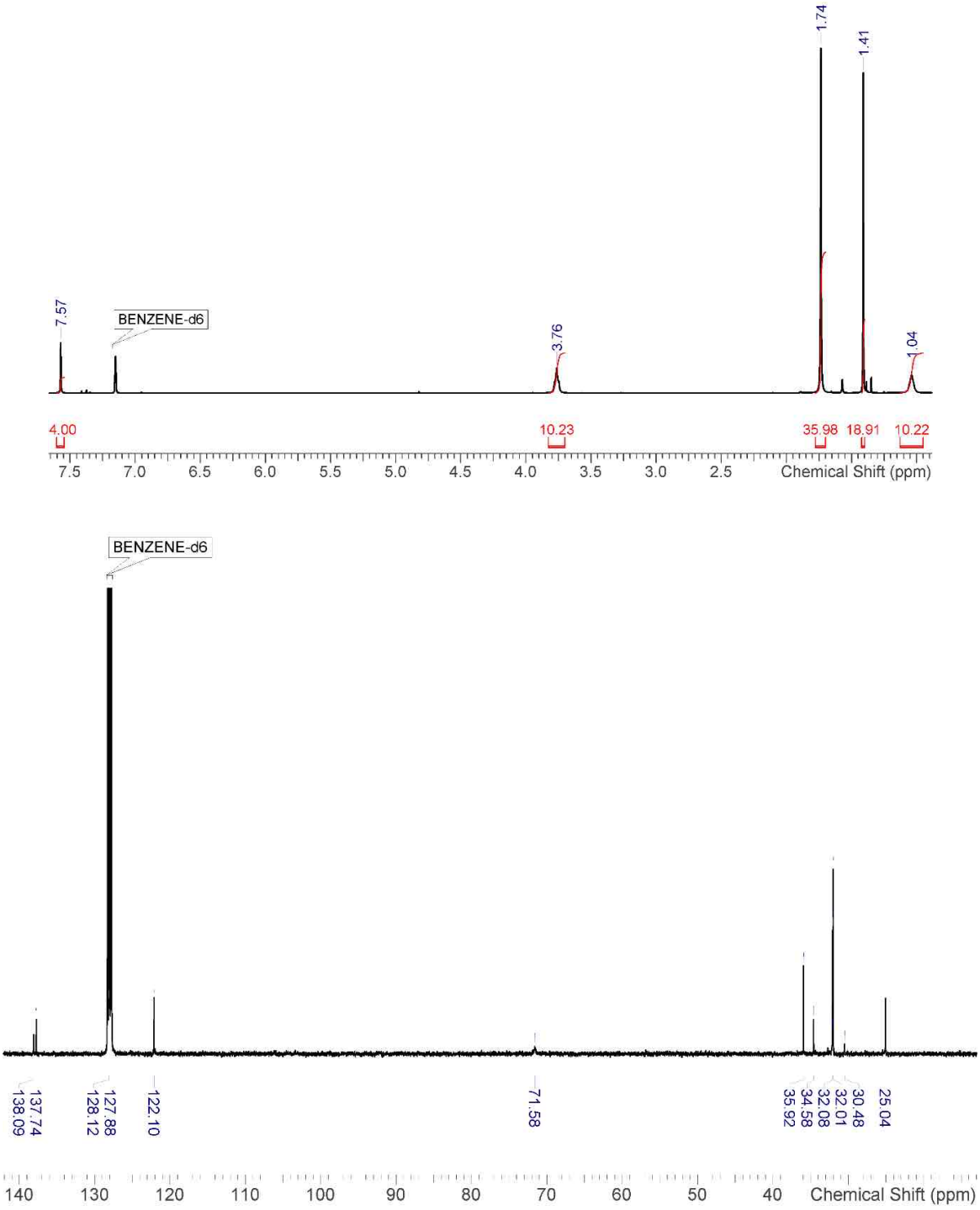

Figure S15. ^{1}H NMR (top) and ^{13}C NMR (bottom) spectrum of **1-Y** [$Y(OMes^*)_2(THF)_2Cl$] in benzene-d_6. For ^{1}H NMR, integrals at 3.76 and 1.04 show partially desolvated compound.

5. IR spectra

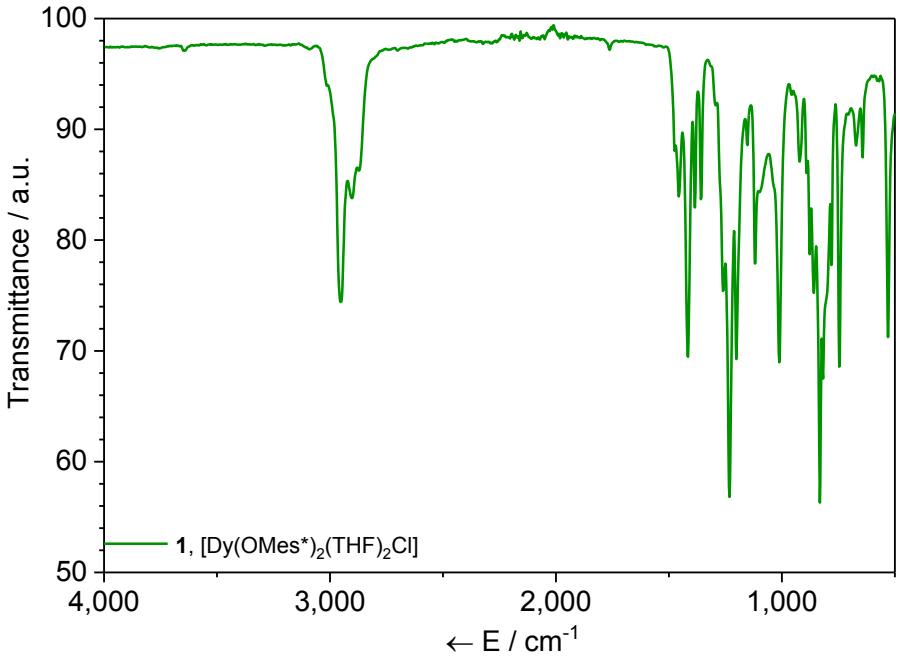

Figure S16. ATIR spectrum of **1**, 394-4000 cm^{-1}.

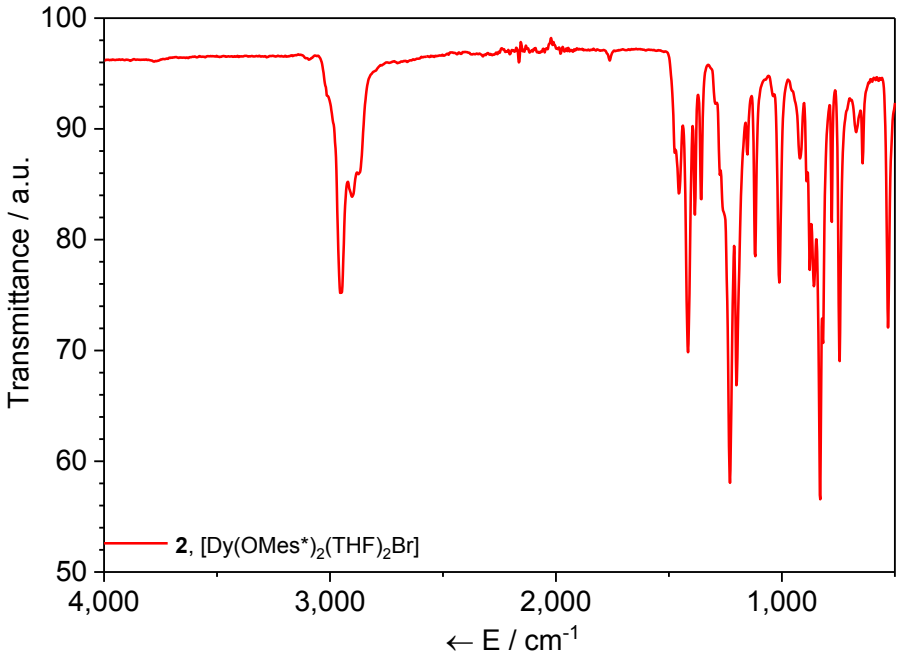

Figure S17. ATIR spectrum of **2**, 394-4000 cm^{-1}.

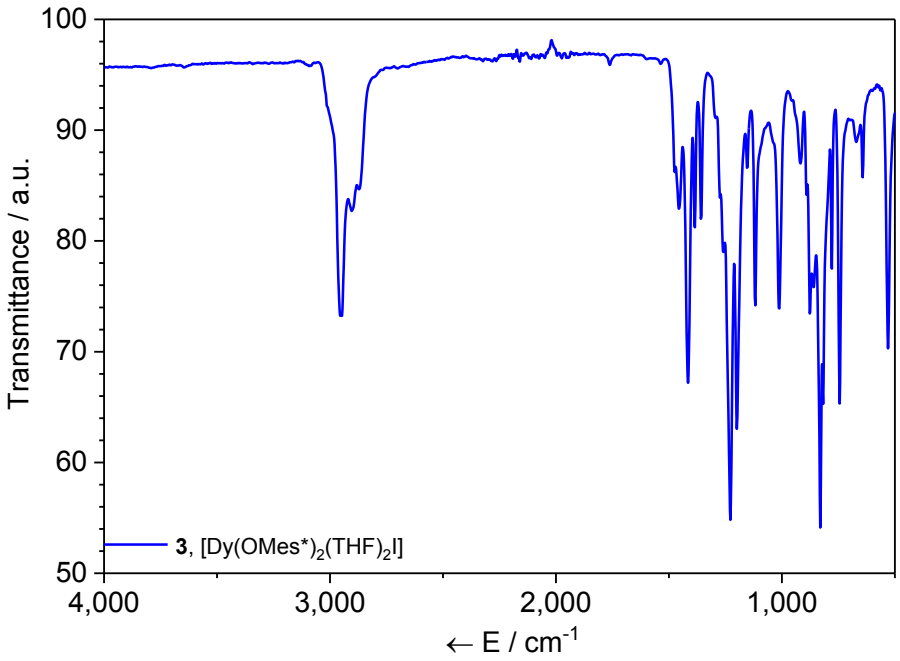

Figure S18. ATIR spectrum of **3**, 394-4000 cm^{-1}

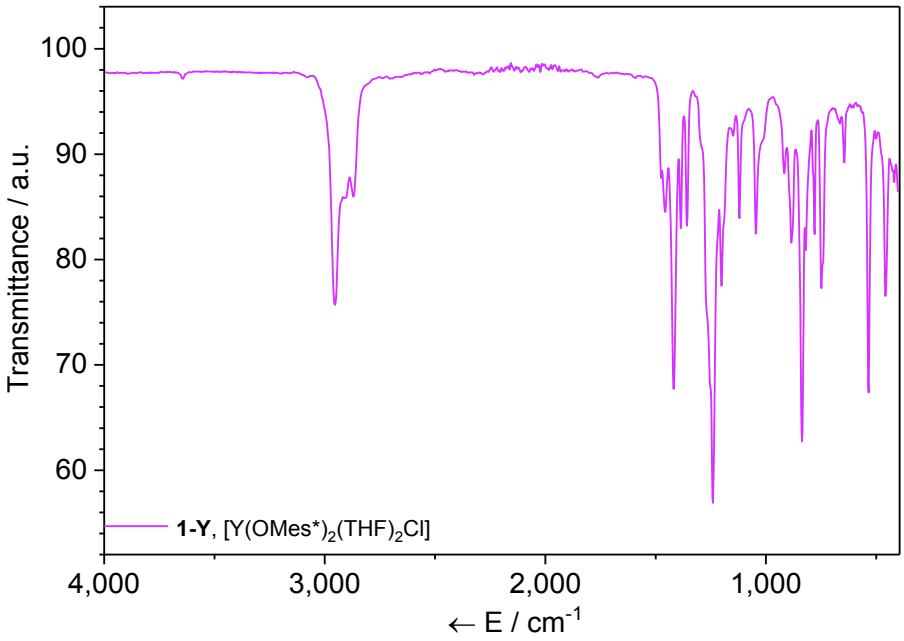

Figure S19. ATIR spectrum of **1-Y**, 394-4000 cm^{-1}.

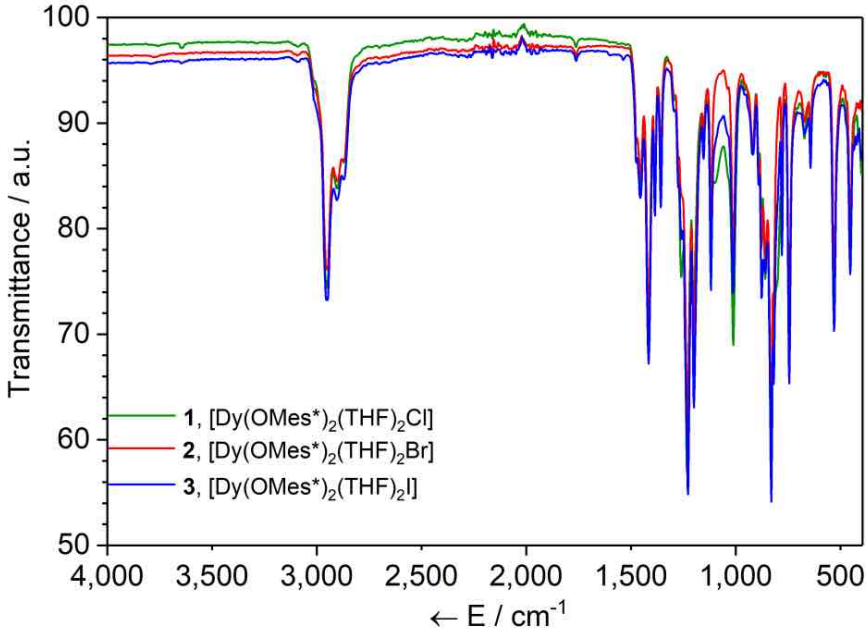

Figure S20. ATIR spectrum of **1-3**, 394-4000 cm^{-1}.

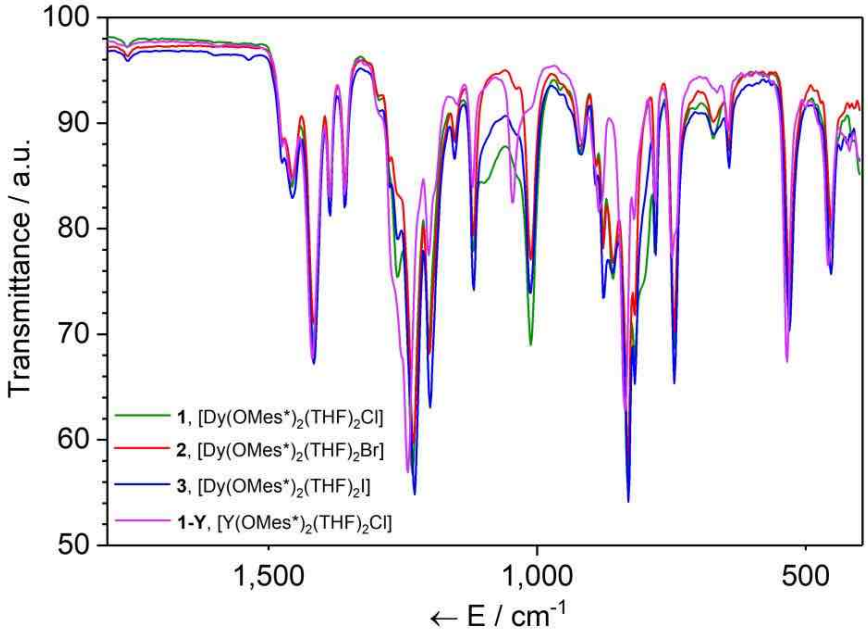

Figure S21. ATIR spectrum of **1-3** and **1-Y**, 394-1800 cm^{-1}.

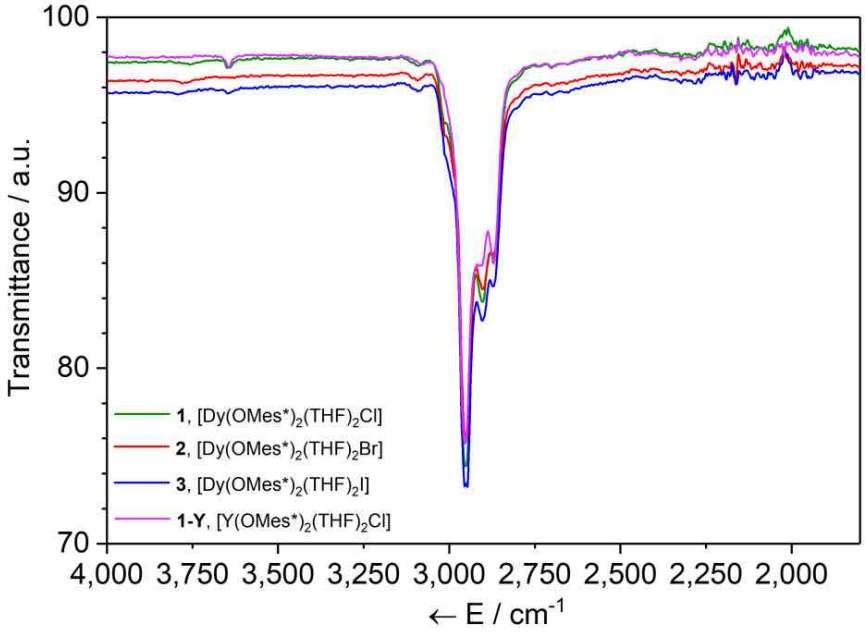

Figure S22. ATIR spectrum of **1-3** and **1-Y**, 1800-4000 cm^{-1}.

6. Computational details

All the first-principle complete active space self-consistent field spin-orbit (CASSCF-SO) calculations have been performed with MOLCAS 8.0[10] software package. The coordinates obtained from single-crystal X-ray structure were used without optimisation. In the active space, we have performed state-average CASSCF calculations with nine electrons in the 7 4f orbitals (i.e. CAS(9,7)) for 21, 224 and 490 roots for the sextet, quartet and doublet spin states, respectively. The ANO-RCC basis set library[11,12] has been used for all the atoms ([ANO-RCC-VTZP] for Dy, [ANO-RCC-VDZP] for O, and [ANO-RCC-VDZ] for C and H) with scalar relativistic effects accounted using the second-order Douglas–Kroll–Hess transformation. The crystal field decomposition of the ground J = 15/2 multiplet of the ^{6}H term was performed using the SINGLE_ANISO[13] module.

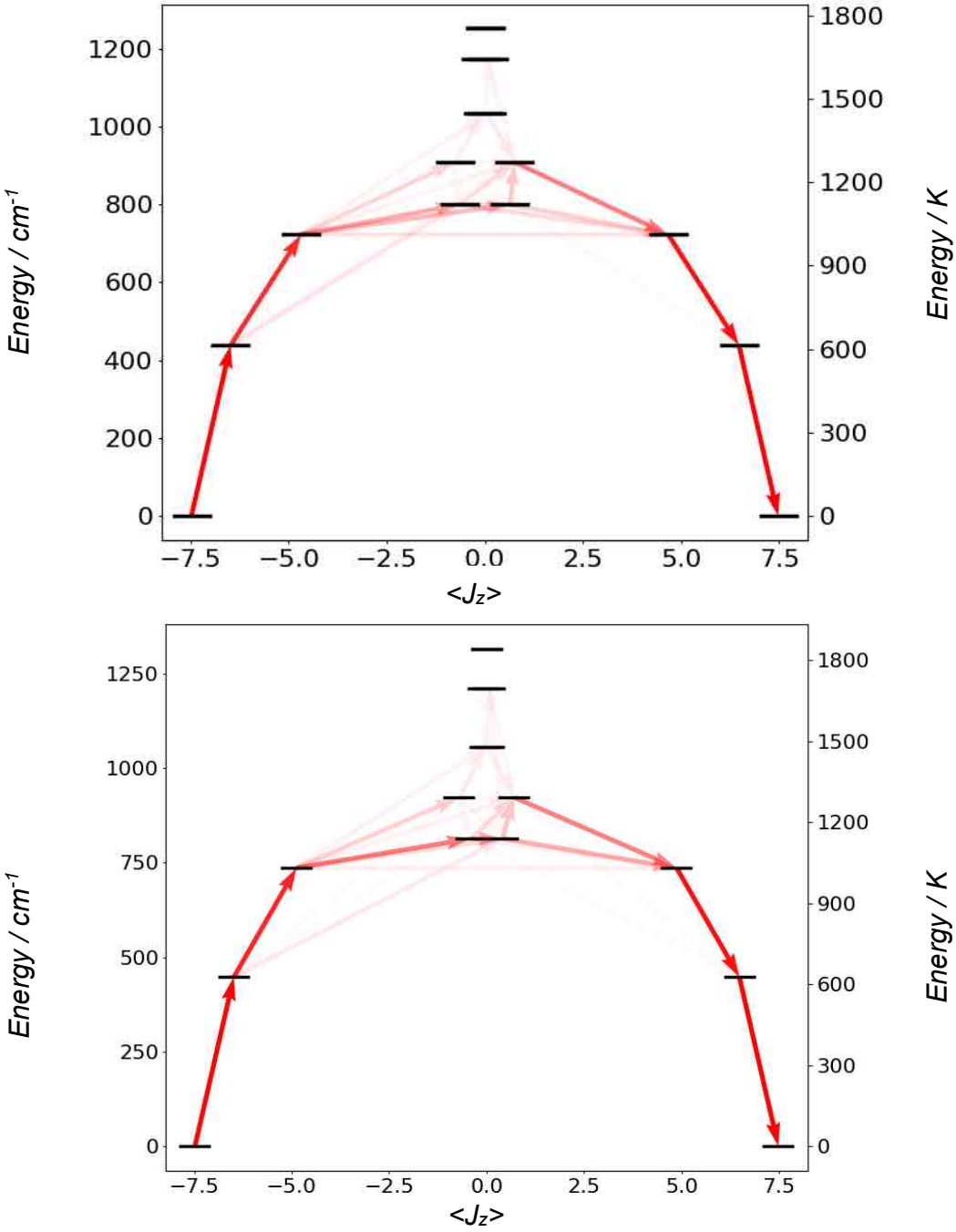

Figure S23. CASSCF-SO-calculated energy diagram of the ground-state multiplet for **2** (top) and **3** (bottom) indicating the zero-field magnetic transition propensities obtained from the average of the three Cartesian transition magnetic moment operators. The opacity of each arrow is proportional to the normalised transition propensity.

Table S6: *Ab initio* results for the *J* = 15/2 multiplet of Dy(III) in **1**, **2** and **3**.

	***Ab initio* Energy (cm^{-1})**	g_x	g_y	g_z	g_z **Angle (º)**	**Wavefunction**
1	0.00	0.00	0.00	19.86	--	99.2%|±15/2⟩
	414.32	0.02	0.02	16.98	0.78	98.3%|±13/2⟩
	689.40	0.96	2.25	13.11	7.38	86.3%|±11/2⟩ + 3.5%|±7/2⟩ + 6.8%|±3/2⟩ + 1.6%|±1/2⟩
	763.94	1.83	4.40	13.26	86.37	8.1%|±11/2⟩ + 20.2%|±9/2⟩ + 5.2%|±7/2⟩ + 19.6%|±5/2⟩ + 14.2%|±3/2⟩ + 32.6%|±1/2⟩
	860.54	3.58	5.10	9.26	87.85	3.2%|±11/2⟩ + 54.1%|±9/2⟩ + 19%|±7/2⟩ + 2.6%|±5/2⟩ + 18.1%|±3/2⟩ + 2.8%|±1/2⟩
	962.24	0.19	0.73	13.68	88.57	21.4%|±9/2⟩ + 45.5%|±7/2⟩ + 24.5%|±5/2⟩ + 7.5%|±1/2⟩
	1073.46	0.32	0.44	16.57	89.16	3.2%|±9/2⟩ + 24.9%|±7/2⟩ + 38.4%|±5/2⟩ + 27%|±3/2⟩ + 5.9%|±1/2⟩
	1113.22	0.04	0.13	19.13	87.44	1.8%|±7/2⟩ + 13.5%|±5/2⟩ + 33.7%|±3/2⟩ + 49.6%|±1/2⟩
2	0.00	0.00	0.00	19.87	--	97.9%|±15/2⟩ + 2%|±13/2⟩
	437.24	0.01	0.01	16.99	1.54	1.8%|±15/2⟩ + 95.1%|±13/2⟩ + 2.6%|±11/2⟩
	722.14	1.09	2.59	13.01	16.25	1.8%|±13/2⟩ + 80.3%|±11/2⟩ + 6.8%|±7/2⟩ + 1.5%|±5/2⟩ + 7%|±3/2⟩ + 2.1%|±1/2⟩
	799.26	1.86	4.65	12.15	82.20	9.7%|±11/2⟩ + 21.9%|±9/2⟩ + 3.6%|±7/2⟩ + 21.1%|±5/2⟩ + 13.4%|±3/2⟩ + 29.7%|±1/2⟩
	906.73	3.13	5.05	9.52	88.64	4.9%|±11/2⟩ + 50%|±9/2⟩ + 17.7%|±7/2⟩ + 3.5%|±5/2⟩ + 19.3%|±3/2⟩ + 4.5%|±1/2⟩
	1033.04	0.45	0.74	13.74	89.15	1.8%|±11/2⟩ + 23%|±9/2⟩ + 44%|±7/2⟩ + 20%|±5/2⟩ + 10.7%|±1/2⟩
	1174.18	0.21	0.30	16.72	89.97	4.5%|±9/2⟩ + 25.2%|±7/2⟩ + 38.8%|±5/2⟩ + 26.2%|±3/2⟩ + 4.8%|±1/2⟩
	1250.97	0.02	0.07	19.41	88.17	2.6%|±7/2⟩ + 14.7%|±5/2⟩ + 33.7%|±3/2⟩ + 48.2%|±1/2⟩
3	0.00	0.00	0.00	19.87	--	98.3%|±15/2⟩ + 1.6%|±13/2⟩
	446.05	0.01	0.01	17.00	1.88	1.5%|±15/2⟩ + 96.2%|±13/2⟩ + 1.9%|±11/2⟩
	735.66	1.10	2.63	12.97	14.73	1.3%|±13/2⟩ + 82.5%|±11/2⟩ + 6.7%|±7/2⟩ + 1.1%|±5/2⟩ + 6.2%|±3/2⟩ + 1.9%|±1/2⟩
	813.16	1.89	4.70	12.26	85.36	8.8%|±11/2⟩ + 20.8%|±9/2⟩ + 3.6%|±7/2⟩ + 22.1%|±5/2⟩ + 14.3%|±3/2⟩ + 30.1%|±1/2⟩
	921.49	3.04	4.95	9.59	90.00	4.6%|±11/2⟩ + 50.2%|±9/2⟩ + 17.8%|±7/2⟩ + 3.8%|±5/2⟩ + 19.6%|±3/2⟩ + 3.9%|±1/2⟩
	1055.76	0.44	0.73	13.74	90.00	1.8%|±11/2⟩ + 23.7%|±9/2⟩ + 43.2%|±7/2⟩ + 18.8%|±5/2⟩ + 12.1%|±1/2⟩
	1211.77	0.18	0.25	16.65	90.00	4.9%|±9/2⟩ + 26%|±7/2⟩ + 39.2%|±5/2⟩ + 25.8%|±3/2⟩ + 3.8%|±1/2⟩
	1314.32	0.02	0.05	19.48	90.00	2.7%|±7/2⟩ + 14.8%|±5/2⟩ + 33.9%|±3/2⟩ + 48.3%|±1/2⟩

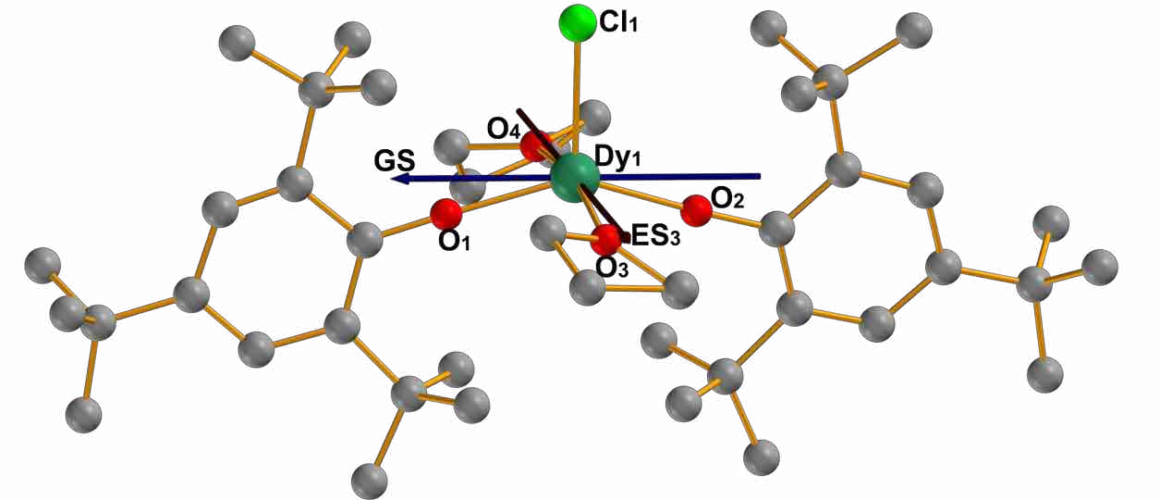

Figure S24: View of the [Dy(OMes*)$_2$(THF)$_2$Cl] molecular structure in **1** with the CASSCF-SO calculated magnetic axis (Gz vector) shown as blue arrow for the ground state and maroon arrow for the fourth state (Dy turquoise, Cl green, O red, C grey). H atoms are omitted for clarity.

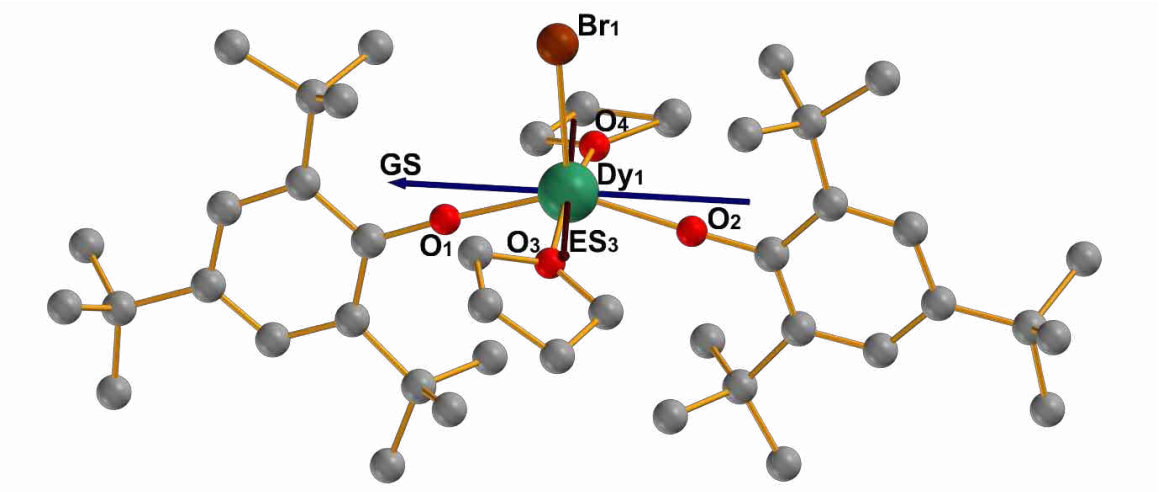

Figure S25: View of the [Dy(OMes*)$_2$(THF)$_2$Br] molecular structure in **2** with the CASSCF-SO calculated magnetic axis (Gz vector) shown as blue arrow for the ground state and maroon arrow for the fourth state (Dy turquoise, Cl green, O red, C grey). H atoms are omitted for clarity.

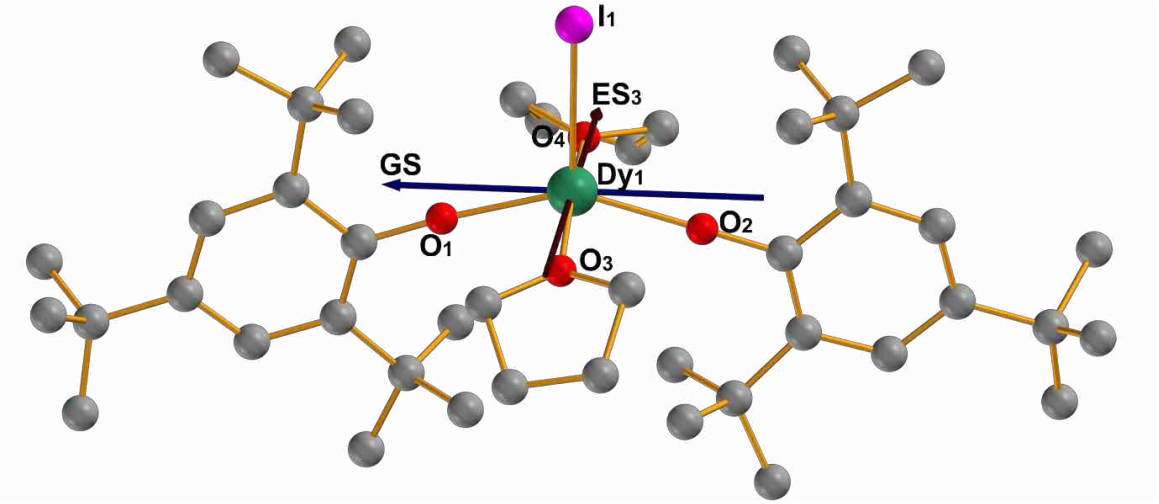

Figure S26: View of the [Dy(OMes*)$_2$(THF)$_2$I] molecular structure in **3** with the CASSCF-SO calculated magnetic axis (Gz vector) shown as blue arrow for the ground state and maroon arrow for the fourth state (Dy turquoise, Cl green, O red, C grey). H atoms are omitted for clarity.

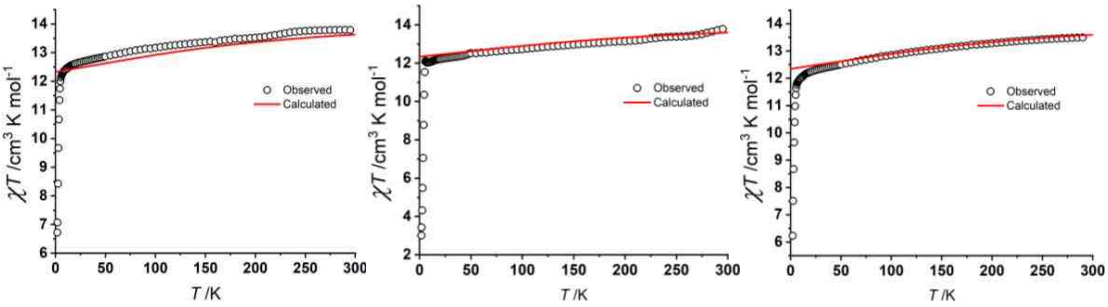

Figure S27. Experimental (black circles) and the CASSCF-SO calculated (red line) temperature dependence of the χT product between 0 and 300 K **1** (left), **2** (centre) and **3** (right). χ is defined as magnetic susceptibility equal to M/H per mole. The experimental χT product is observed at 0.1 T field. The plots show the experimental and theoretical agreement for compounds **1**, **2**, and **3**.

Table S7: Average transition magnetic moment elements between the states on **1**.

	1	2	3	4	5	6	7	8	9	10	11	12	13	14	15	16
1		0.0000	3.6330	0.0028	0.0002	0.0067	0.0065	0.0027	0.0126	0.0034	0.0034	0.0032	0.0004	0.0016	0.0003	0.0003
2	0.0000		0.0028	3.6330	0.0067	0.0002	0.0027	0.0065	0.0034	0.0126	0.0032	0.0034	0.0016	0.0004	0.0003	0.0003
3	3.6330	0.0028		0.0621	0.0093	6.0570	0.0352	0.4188	0.0133	0.1460	0.0847	0.0158	0.0126	0.0193	0.0047	0.0051
4	0.0028	3.6330	0.0621		6.0570	0.0093	0.4188	0.0352	0.1460	0.0133	0.0158	0.0847	0.0193	0.0126	0.0051	0.0047
5	0.0002	0.0067	0.0093	6.0570		0.4284	2.1340	5.4030	0.4023	2.9740	0.8196	0.0273	0.0192	0.1976	0.0319	0.0231
6	0.0067	0.0002	6.0570	0.0093	0.4284		5.4030	2.1340	2.9740	0.4023	0.0273	0.8196	0.1976	0.0192	0.0231	0.0319
7	0.0065	0.0027	0.0352	0.4188	2.1340	5.4030		9.3600	3.9620	4.2700	0.0927	0.0559	0.0339	0.0708	0.0463	0.0330
8	0.0027	0.0065	0.4188	0.0352	5.4030	2.1340	9.3600		4.2700	3.9620	0.0559	0.0927	0.0708	0.0339	0.0330	0.0463
9	0.0126	0.0034	0.0133	0.1460	0.4023	2.9740	3.9620	4.2700		6.1620	5.7790	4.0630	0.0171	0.1405	0.0928	0.2192
10	0.0034	0.0126	0.1460	0.0133	2.9740	0.4023	4.2700	3.9620	6.1620		4.0630	5.7790	0.1405	0.0171	0.2192	0.0928
11	0.0034	0.0032	0.0847	0.0158	0.8196	0.0273	0.0927	0.0559	5.7790	4.0630		11.7600	3.9770	2.5750	0.1991	0.1295
12	0.0032	0.0034	0.0158	0.0847	0.0273	0.8196	0.0559	0.0927	4.0630	5.7790	11.7600		2.5750	3.9770	0.1295	0.1991
13	0.0004	0.0016	0.0126	0.0193	0.0192	0.1976	0.0339	0.0708	0.0171	0.1405	3.9770	2.5750		18.7100	1.7010	3.1010
14	0.0016	0.0004	0.0193	0.0126	0.1976	0.0192	0.0708	0.0339	0.1405	0.0171	2.5750	3.9770	18.7100		3.1010	1.7010
15	0.0003	0.0003	0.0047	0.0051	0.0319	0.0231	0.0463	0.0330	0.0928	0.2192	0.1991	0.1295	1.7010	3.1010		19.5400
16	0.0003	0.0003	0.0051	0.0047	0.0231	0.0319	0.0330	0.0463	0.2192	0.0928	0.1295	0.1991	3.1010	1.7010	19.5400	

Table S8: Average transition magnetic moment elements between the states on **2**.

	1	**2**	**3**	**4**	**5**	**6**	**7**	**8**	**9**	**10**	**11**	**12**	**13**	**14**	**15**	**16**
1		0.0000	3.6000	0.0000	0.0090	0.0000	0.0060	0.0020	0.0120	0.0030	0.0020	0.0040	0.0010	0.0010	0.0000	0.0000
2	0.0000		0.0000	3.6000	0.0000	0.0090	0.0020	0.0060	0.0030	0.0120	0.0040	0.0020	0.0010	0.0010	0.0000	0.0000
3	3.6000	0.0000		0.0000	5.9370	0.0030	0.0520	0.4730	0.0130	0.1890	0.0920	0.0110	0.0210	0.0090	0.0020	0.0030
4	0.0000	3.6000	0.0000		0.0030	5.9370	0.4730	0.0520	0.1890	0.0130	0.0110	0.0920	0.0090	0.0210	0.0030	0.0020
5	0.0090	0.0000	5.9370	0.0030		0.4960	4.1200	3.9950	2.2520	0.9300	0.0840	0.6430	0.0110	0.1560	0.0120	0.0130
6	0.0000	0.0090	0.0030	5.9370	0.4960		3.9950	4.1200	0.9300	2.2520	0.6430	0.0840	0.1560	0.0110	0.0130	0.0120
7	0.0060	0.0020	0.0520	0.4730	4.1200	3.9950		2.5650	3.2810	5.4120	0.1000	0.0250	0.0470	0.0360	0.0100	0.0350
8	0.0020	0.0060	0.4730	0.0520	3.9950	4.1200	2.5650		5.4120	3.2810	0.0250	0.1000	0.0360	0.0470	0.0350	0.0100
9	0.0120	0.0030	0.0130	0.1890	2.2520	0.9300	3.2810	5.4120		7.3710	6.4860	3.2820	0.0710	0.0200	0.0850	0.0330
10	0.0030	0.0120	0.1890	0.0130	0.9300	2.2520	5.4120	3.2810	7.3710		3.2820	6.4860	0.0200	0.0710	0.0330	0.0850
11	0.0020	0.0040	0.0920	0.0110	0.0840	0.6430	0.1000	0.0250	6.4860	3.2820		12.3400	2.8460	4.1350	0.0430	0.0450
12	0.0040	0.0020	0.0110	0.0920	0.6430	0.0840	0.0250	0.1000	3.2820	6.4860	12.3400		4.1350	2.8460	0.0450	0.0430
13	0.0010	0.0010	0.0210	0.0090	0.0110	0.1560	0.0470	0.0360	0.0710	0.0200	2.8460	4.1350		18.8500	1.2290	3.1390
14	0.0010	0.0010	0.0090	0.0210	0.1560	0.0110	0.0360	0.0470	0.0200	0.0710	4.1350	2.8460	18.8500		3.1390	1.2290
15	0.0000	0.0000	0.0020	0.0030	0.0120	0.0130	0.0100	0.0350	0.0850	0.0330	0.0430	0.0450	1.2290	3.1390		25.4000
16	0.0000	0.0000	0.0030	0.0020	0.0130	0.0120	0.0350	0.0100	0.0330	0.0850	0.0450	0.0430	3.1390	1.2290	25.4000	

Table S9: Average transition magnetic moment elements between the states on **3**.

	1	**2**	**3**	**4**	**5**	**6**	**7**	**8**	**9**	**10**	**11**	**12**	**13**	**14**	**15**	**16**
1		0.0000	0.1074	4.3350	0.0107	0.0002	0.0020	0.0082	0.0044	0.0151	0.0057	0.0027	0.0016	0.0008	0.0004	0.0000
2	0.0000		4.3350	0.1074	0.0002	0.0107	0.0082	0.0020	0.0151	0.0044	0.0027	0.0057	0.0008	0.0016	0.0000	0.0004
3	0.1074	4.3350		2.3510	0.1809	7.0660	0.0633	0.6639	0.0229	0.2359	0.1175	0.0111	0.0102	0.0267	0.0055	0.0015
4	4.3350	0.1074	2.3510		7.0660	0.1809	0.6639	0.0633	0.2359	0.0229	0.0111	0.1175	0.0267	0.0102	0.0015	0.0055
5	0.0107	0.0002	0.1809	7.0660		0.7021	4.7250	5.6910	1.2480	2.5330	0.8487	0.0369	0.0105	0.1943	0.0160	0.0136
6	0.0002	0.0107	7.0660	0.1809	0.7021		5.6910	4.7250	2.5330	1.2480	0.0369	0.8487	0.1943	0.0105	0.0136	0.0160
7	0.0020	0.0082	0.0633	0.6639	4.7250	5.6910		4.0520	4.2730	6.5610	0.1265	0.0394	0.0345	0.0670	0.0088	0.0470
8	0.0082	0.0020	0.6639	0.0633	5.6910	4.7250	4.0520		6.5610	4.2730	0.0394	0.1265	0.0670	0.0345	0.0470	0.0088
9	0.0044	0.0151	0.0229	0.2359	1.2480	2.5330	4.2730	6.5610		9.0710	7.9340	4.1030	0.0200	0.0891	0.1060	0.0381
10	0.0151	0.0044	0.2359	0.0229	2.5330	1.2480	6.5610	4.2730	9.0710		4.1030	7.9340	0.0891	0.0200	0.0381	0.1060
11	0.0057	0.0027	0.1175	0.0111	0.8487	0.0369	0.1265	0.0394	7.9340	4.1030		15.7900	5.4970	3.1220	0.1059	0.0002
12	0.0027	0.0057	0.0111	0.1175	0.0369	0.8487	0.0394	0.1265	4.1030	7.9340	15.7900		3.1220	5.4970	0.0002	0.1059
13	0.0016	0.0008	0.0102	0.0267	0.0105	0.1943	0.0345	0.0670	0.0200	0.0891	5.4970	3.1220		23.3300	1.1790	4.1950
14	0.0008	0.0016	0.0267	0.0102	0.1943	0.0105	0.0670	0.0345	0.0891	0.0200	3.1220	5.4970	23.3300		4.1950	1.1790
15	0.0004	0.0000	0.0055	0.0015	0.0160	0.0136	0.0088	0.0470	0.1060	0.0381	0.1059	0.0002	1.1790	4.1950		32.0600
16	0.0000	0.0004	0.0015	0.0055	0.0136	0.0160	0.0470	0.0088	0.0381	0.1060	0.0002	0.1059	4.1950	1.1790	32.0600	

Table S10: Crystal field parameters in **1**, **2** and **3**.

k	*q*	*B*(*k,q*) **1**	*B*(*k,q*) **2**	*B*(*k,q*) **3**
2	-2	1.50E+00	-1.02E-01	-4.01E-04
2	-1	3.39E-01	1.49E+00	1.43E+00
2	0	-5.58E+00	-6.11E+00	-6.34E+00
2	1	-5.62E-01	6.39E-02	9.09E-05
2	2	-1.90E+00	3.45E+00	3.89E+00
4	-4	2.63E-02	-3.86E-03	5.92E-06
4	-3	-1.60E-02	2.93E-02	2.57E-02
4	-2	-1.28E-02	-1.19E-04	3.83E-06
4	-1	1.23E-03	2.10E-02	1.92E-02
4	0	-9.27E-03	-8.98E-03	-8.87E-03
4	1	-1.03E-02	-2.67E-03	2.03E-06
4	2	1.79E-02	-2.17E-02	-2.37E-02
4	3	2.23E-03	-1.75E-04	4.53E-06
4	4	-4.02E-03	-2.43E-02	-2.17E-02
6	-6	-1.23E-04	-1.55E-05	6.12E-08
6	-5	1.38E-04	2.68E-04	2.44E-04
6	-4	1.23E-04	-1.84E-05	3.33E-08
6	-3	-7.86E-05	1.15E-04	1.14E-04
6	-2	-5.24E-05	-3.12E-06	9.05E-09
6	-1	1.56E-05	-1.92E-07	2.03E-05
6	0	9.30E-06	9.59E-06	8.94E-06
6	1	2.66E-06	1.13E-05	2.50E-09
6	2	5.81E-05	-6.50E-05	-5.43E-05
6	3	-5.52E-07	-2.10E-07	2.44E-08
6	4	-1.87E-05	-1.15E-04	-1.14E-04
6	5	5.68E-05	-5.32E-05	6.47E-08
6	6	-5.10E-05	-1.58E-04	-1.53E-04

7. Magnetism

Magnetic susceptibility measurements were performed on a Quantum Design SQUID MPMS-XL magnetometer and PPMS-II susceptometer housed at the Centre de Recherche Paul Pascal at temperatures between 1.8 and 400 K and *dc* magnetic fields ranging from -9 to +9 T. The *ac* magnetic susceptibility measurements were performed in an oscillating *ac* field of 1 to 6 Oe with frequencies between 10 and 10000 Hz in zero *dc*-field. The measurements were carried out on polycrystalline samples (12.4, 7.3, 9.1, 34.0 and 32.5 for **1**, 12.5 mg for **2**, 9.3 mg for **3** and 33.5 and 35.2 mg for **5%Dy@1-Y**) suspended in mineral oil (typically 7-19 mg) and introduced in a sealed polyethene bag (3 $\times$ 0.5 $\times$ 0.02 cm; typically, 13-31 mg) in a glovebox a controlled atmosphere of nitrogen or argon. Prior to the experiments, the field-dependent magnetisation was measured at 100 K on each sample in order to detect the presence of any bulk ferromagnetic impurities. As expected for paramagnetic or diamagnetic materials, a perfectly linear dependence of the magnetisation that extrapolates to zero at zero *dc* field was systematically observed; the samples appeared to be free of any ferromagnetic impurities. The magnetic susceptibilities were corrected for the sample holder, the mineral oil and the intrinsic diamagnetic contributions.

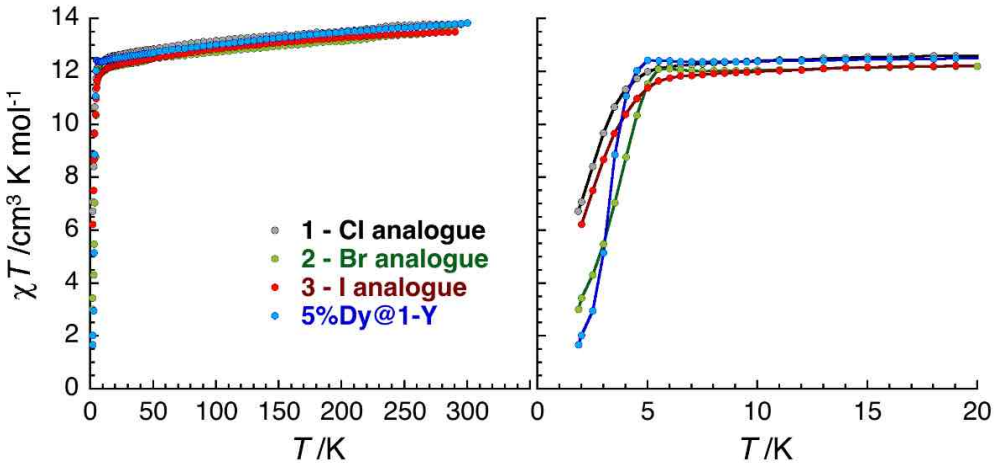

Figure S28. Temperature dependence of the χT product at 0.1 T between 0 and 300 K (left) and 0 and 20 K (right) for **1**, **2**, **3** and **5%Dy@1-Y** at 0.3 K/min. χ is defined as magnetic susceptibility equal to *M*/*H* per mole of complex except for **5%Dy@1-Y**, for which χ has been multiplied by 20, for clarity, according to the 5% Dy dilution. The χT products at 270, 100 and 1.85 K are 13.8, 13.2 and 6.72 cm^3 K/mol for **1**, 13.8, 13.2 and 6.72 cm^3 K/mol for **1**, 13.5, 12.7 and 3.01 cm^3 K/mol for **2**, 13.5, 12.8 and 6.22 cm^3 K/mol for **3** and 13.7, 13.0 and 1.66 cm^3 K/mol for **5%Dy@1-Y**.

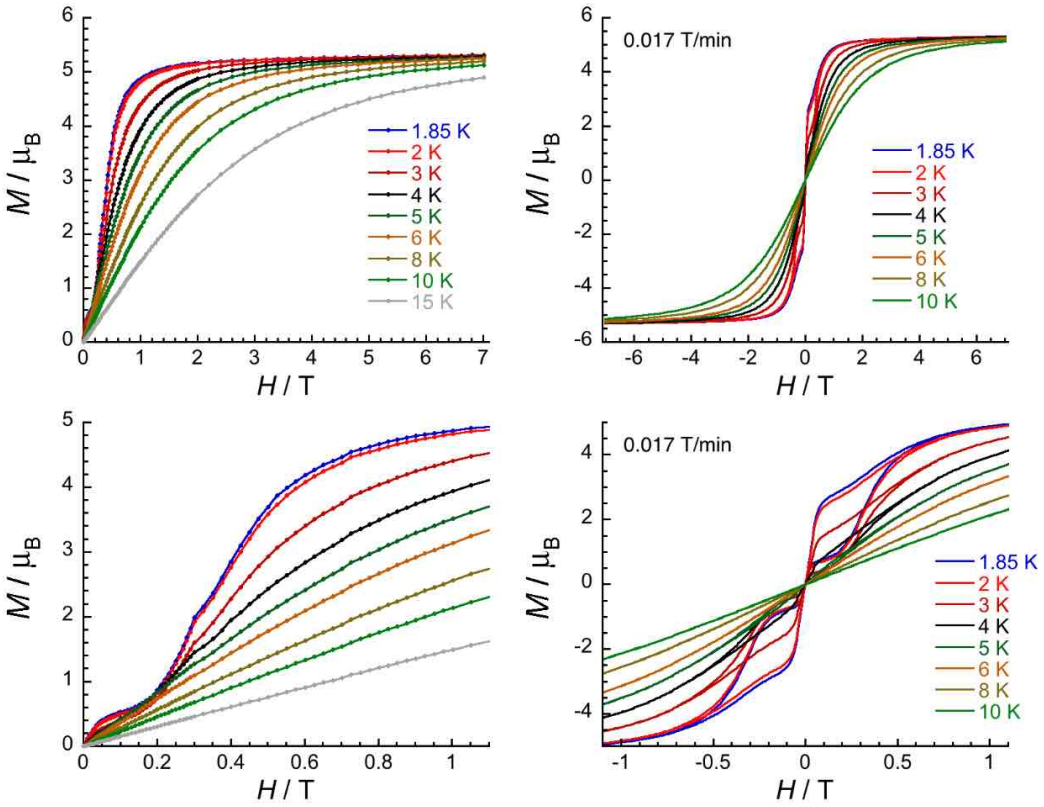

Figure S29. Field dependence of the magnetisation for **1**. On the left, the *M* vs *H* data between 1.85 and 15 K have been measured after a zero-field cooling from 20 K to the indicated temperature in order to obtain first magnetization curves between 0 and 7 T (top); a zoom of these data between 0 and 1.1 T is shown in the bottom part of the figure (field sweeping rates: 9 mT/min between 0 and 0.1 T, 18 mT/min between 0.1 and 0.35 T, 40 mT/min between 0.35 and 1 T, 84 mT/min between 1 and 2 T, 280 mT/min between 2 and 7 T). On the right, the *M* vs *H* data between 1.85 and 10 K have been measured at 17 mT/min after saturating the magnetisation at 7 T (*M*(1.85 K, 7 T) = 5.3 μ_B) in order to obtain magnetisation hysteresis curves between -7 and 7 T (top); a zoom of these data between -1.1 and 1.1 T is shown in the bottom part of the figure.

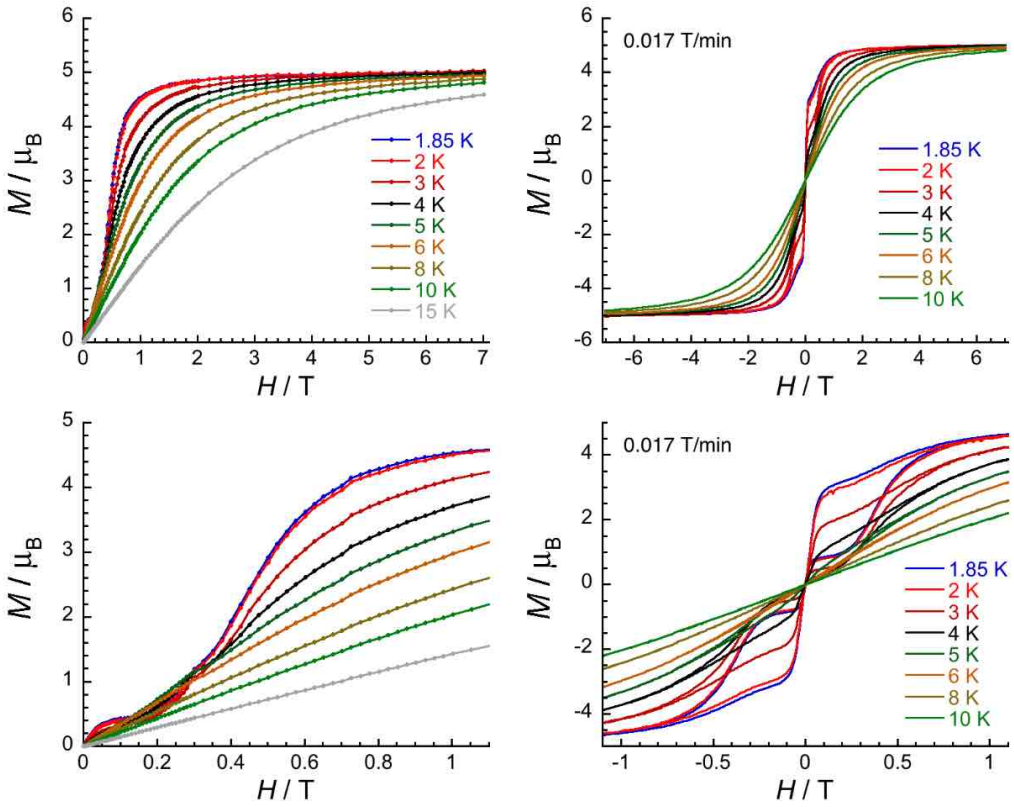

Figure S30. Field dependence of the magnetisation for **2**. On the left, the *M* vs *H* data between 1.85 and 15 K have been measured after a zero-field cooling from 20 K to the indicated temperature in order to obtain first magnetisation curves between 0 and 7 T (top); a zoom of these data between 0 and 1.1 T is shown in the bottom part of the figure (field sweeping rates: 9 mT/min between 0 and 0.1 T, 18 mT/min between 0.1 and 0.35 T, 40 mT/min between 0.35 and 1 T, 84 mT/min between 1 and 2 T, 280 mT/min between 2 and 7 T). On the right, the *M* vs *H* data between 1.85 and 10 K have been measured at 17 mT/min after saturating the magnetisation at 7 T (*M*(1.85 K, 7 T) = 5.0 μ_B) in order to obtain magnetisation hysteresis curves between -7 and 7 T (top); a zoom of these data between -1.1 and 1.1 T is shown in the bottom part of the figure.

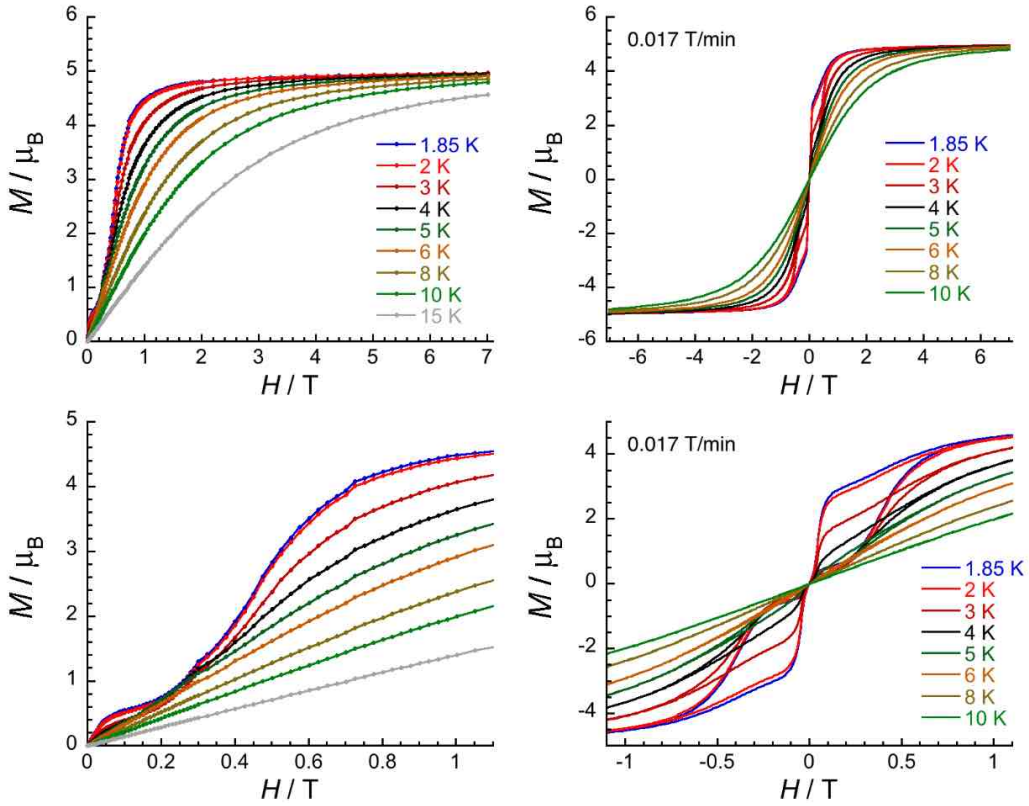

Figure S31. Field dependence of the magnetisation for **3**. On the left, the *M* vs *H* data between 1.85 and 15 K have been measured after a zero-field cooling from 20 K to the indicated temperature in order to obtain first magnetisation curves between 0 and 7 T (top); a zoom of these data between 0 and 1.1 T is shown in the bottom part of the figure (field sweeping rates: 9 mT/min between 0 and 0.1 T, 18 mT/min between 0.1 and 0.35 T, 40 mT/min between 0.35 and 1 T, 84 mT/min between 1 and 2 T, 280 mT/min between 2 and 7 T). On the right, the *M* vs *H* data between 1.85 and 10 K have been measured at 17 mT/min after saturating the magnetisation at 7 T (*M*(1.85 K, 7 T) = 5.0 μ_B) in order to obtain magnetisation hysteresis curves between -7 and 7 T (top); a zoom of these data between -1.1 and 1.1 T is shown in the bottom part of the figure.

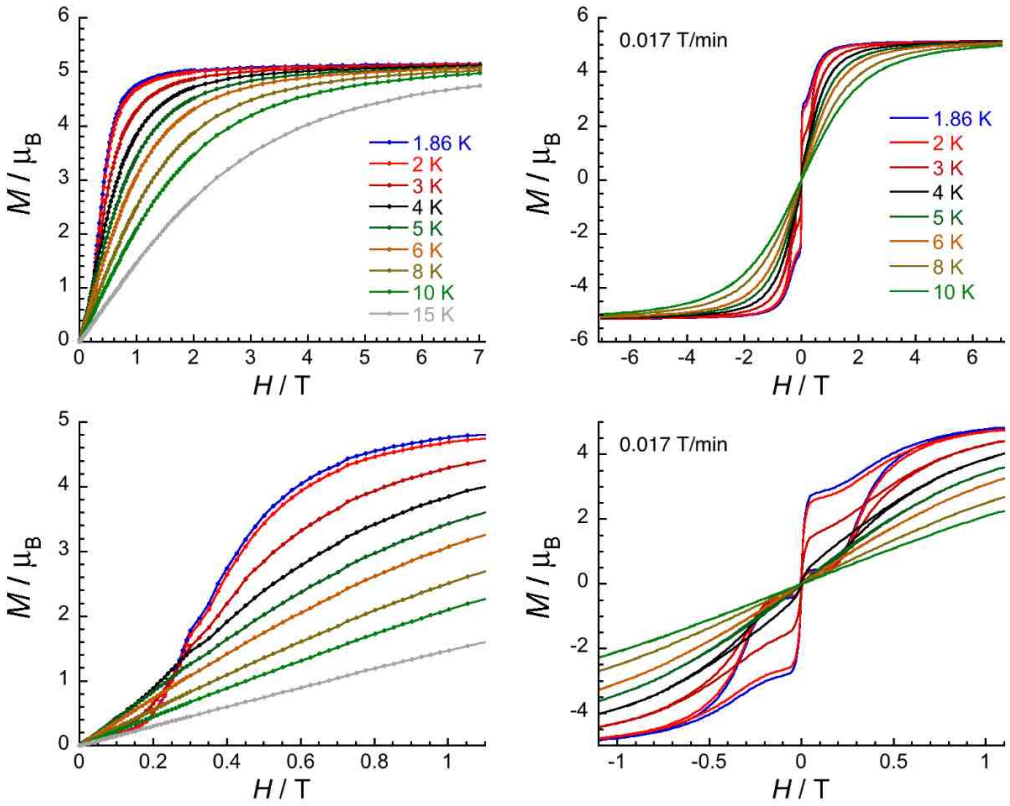

Figure S32. Field dependence of the magnetisation (multiplied by 20 according to the 5% Dy dilution for easier comparison with the other complexes) for **5%Dy@1-Y**. On the left, the *M* vs *H* data between 1.85 and 15 K have been measured after a zero-field cooling from 20 K to the indicated temperature in order to obtain first magnetisation curves between 0 and 7 T (top); a zoom of these data between 0 and 1.1 T is shown in the bottom part of the figure (field sweeping rates: 9 mT/min between 0 and 0.1 T, 18 mT/min between 0.1 and 0.35 T, 40 mT/min between 0.35 and 1 T, 84 mT/min between 1 and 2 T, 280 mT/min between 2 and 7 T). On the right, the *M* vs *H* data between 1.85 and 10 K have been measured at 17 mT/min after saturating the magnetisation at 7 T (M(1.85 K, 7 T) = 5.2 μ_B) in order to obtain magnetisation hysteresis curves between -7 and 7 T (top); a zoom of these data between -1.1 and 1.1 T is shown in the bottom part of the figure.

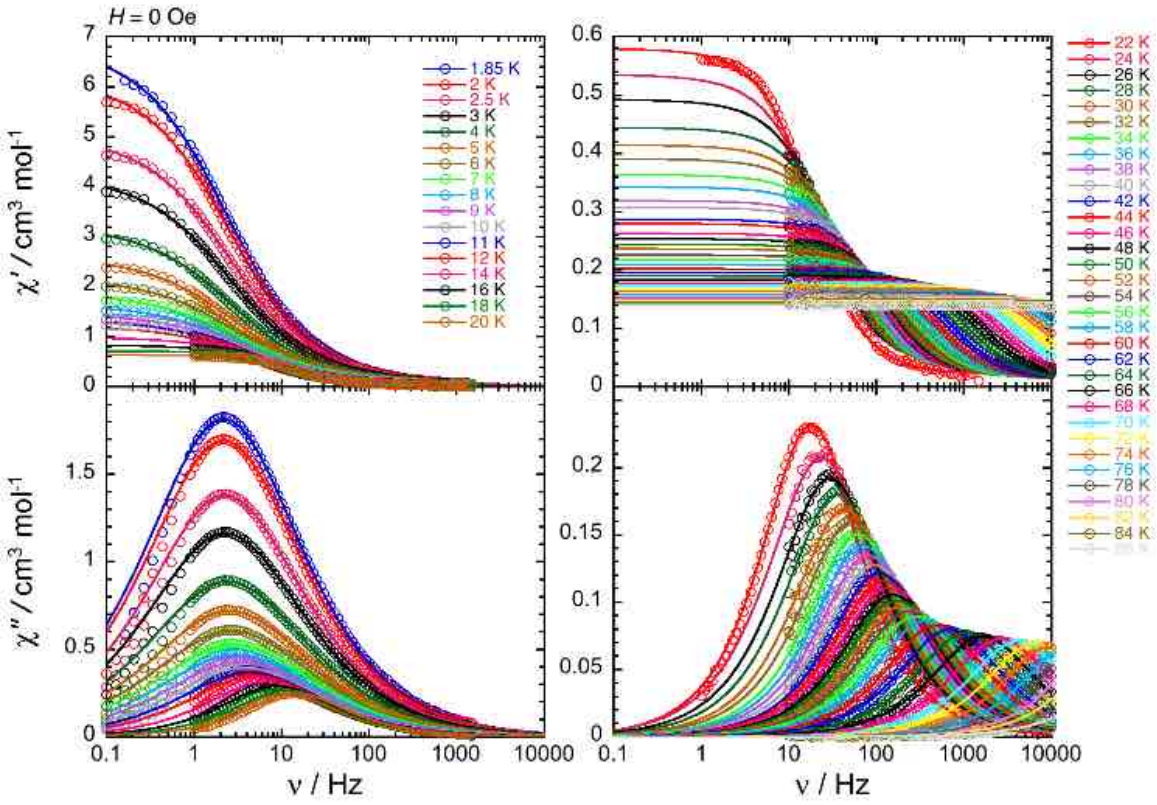

Figure 33. ac frequency dependences of the real (χ', top) and imaginary (χ'', bottom) parts of the ac susceptibility for **1**, between 1.85 and 20 K (left) and between 22 and 86 K (right) for ac frequencies between 0.1 and 10000 Hz (in a zero-dc field). Solid lines are the generalised Debye fit of the ac data used to extract the temperature dependence of the relaxation time.

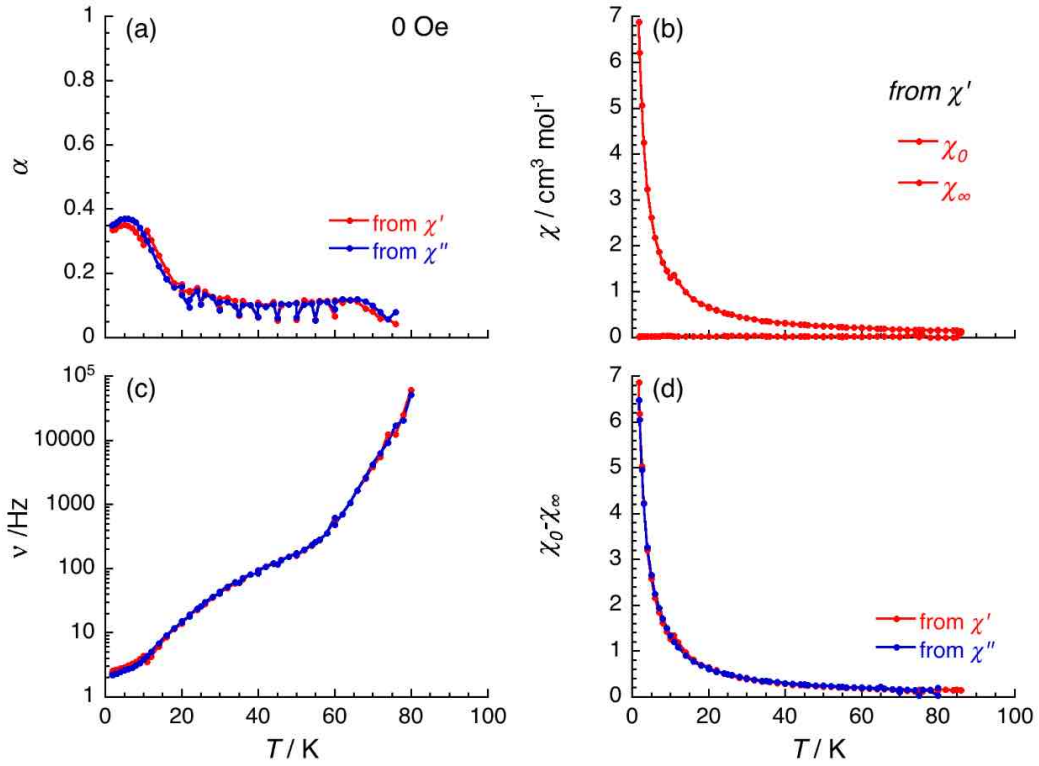

Figure S34. Field dependence of the parameters α, ν, χ_0, χ_∞ and χ_0-χ_∞, between 1.85 and 86 K in zero-dc field deduced from the generalised Debye fit of the frequency dependence of the real (χ') and imaginary (χ'') components of the ac susceptibility shown in Figure S33, for **1**.

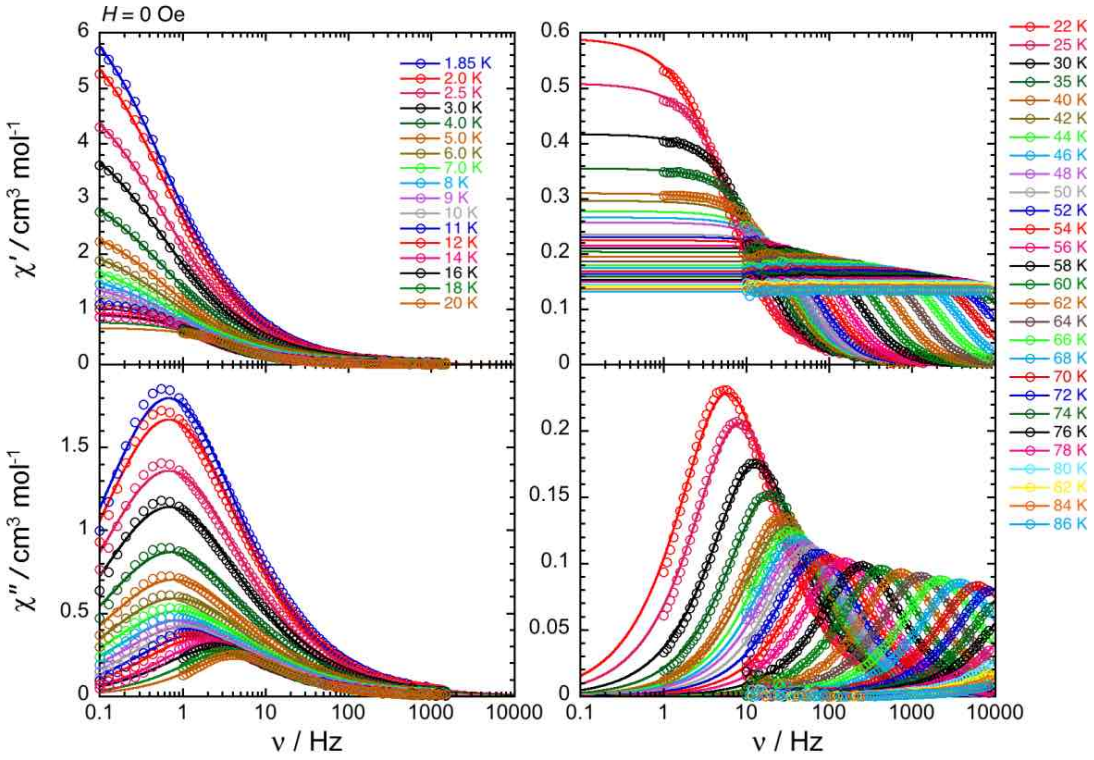

Figure S35. ac frequency dependences of the real (χ', top) and imaginary (χ'', bottom) parts of the ac susceptibility for **2**, between 1.85 and 20 K (left) and between 22 and 86 K (right) for ac frequencies between 0.1 and 10000 Hz (in a zero-dc field). Solid lines are the generalised Debye fit of the ac data used to extract the temperature dependence of the relaxation time.

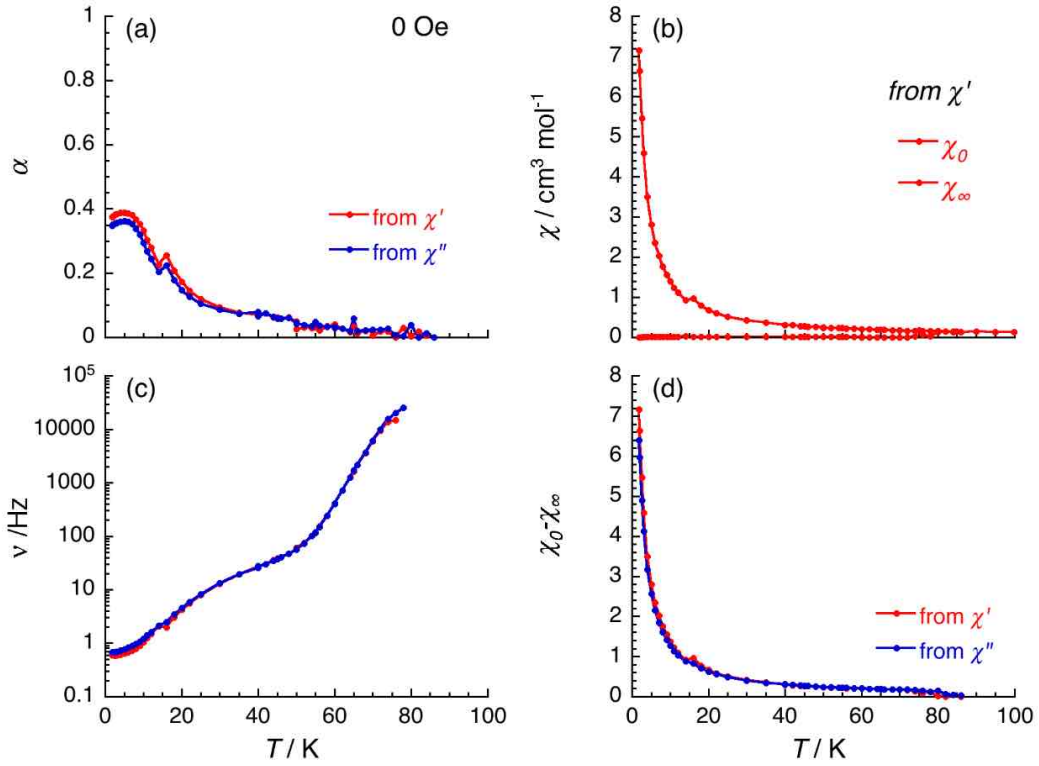

Figure S36. Field dependence of the parameters, α, ν, χ_0, χ_∞ and χ_0-χ_∞, between 1.85 and 86 K in zero-dc field deduced from the generalised Debye fit of the frequency dependence of the real (χ') and imaginary (χ'') components of the ac susceptibility shown in Figure S35, for **2**.

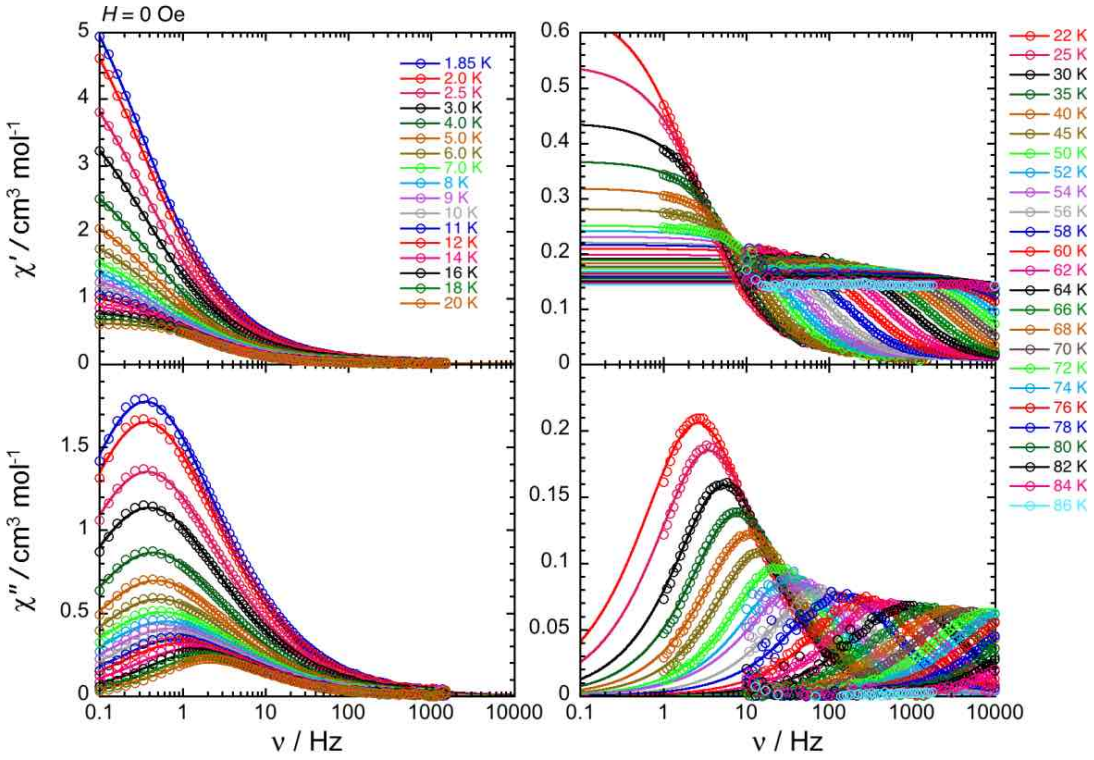

Figure S37. ac frequency dependences of the real (χ', top) and imaginary (χ'', bottom) parts of the ac susceptibility for **3**, between 1.85 and 20 K (left) and between 22 and 86 K (right) for ac frequencies between 0.1 and 10000 Hz (in a zero-dc field). Solid lines are the generalised Debye fit of the ac data used to extract the temperature dependence of the relaxation time.

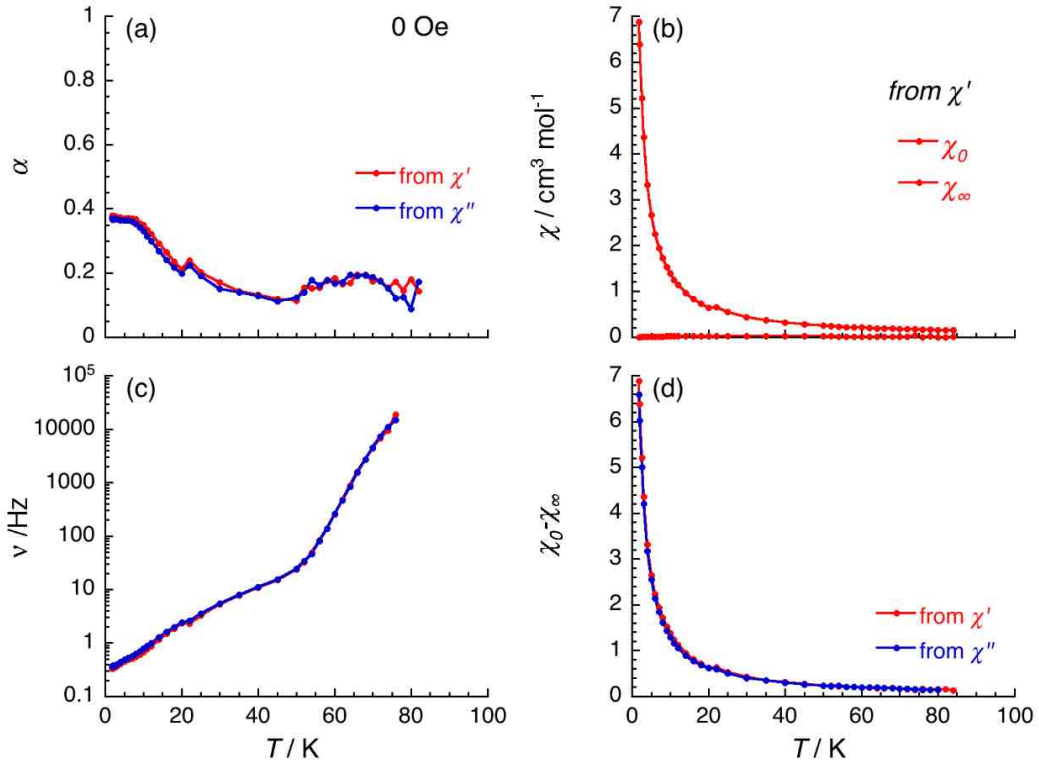

Figure S38. Field dependence of the parameters, α, ν, χ_0, χ_∞ and χ_0-χ_∞, between 1.85 and 86 K in zero-dc field deduced from the generalised Debye fit of the frequency dependence of the real (χ') and imaginary (χ'') components of the ac susceptibility shown in Figure S37, for **3**.

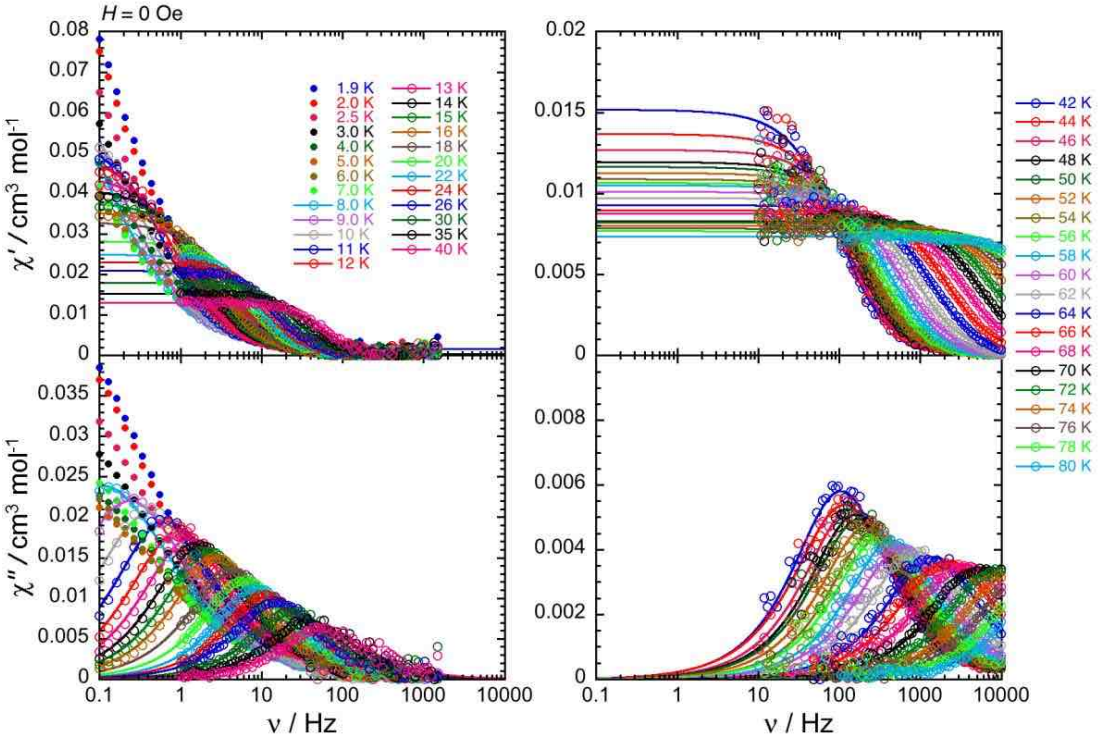

Figure S39. ac frequency dependences of the real (χ', top) and imaginary (χ'', bottom) parts of the ac susceptibility for **5%Dy@1-Y**, between 1.85 and 20 K (left) and between 22 and 86 K (right) for ac frequencies between 0.1 and 10000 Hz (in a zero-dc field). Solid lines are the generalised Debye fit of the ac data used to extract the temperature dependence of the relaxation time.

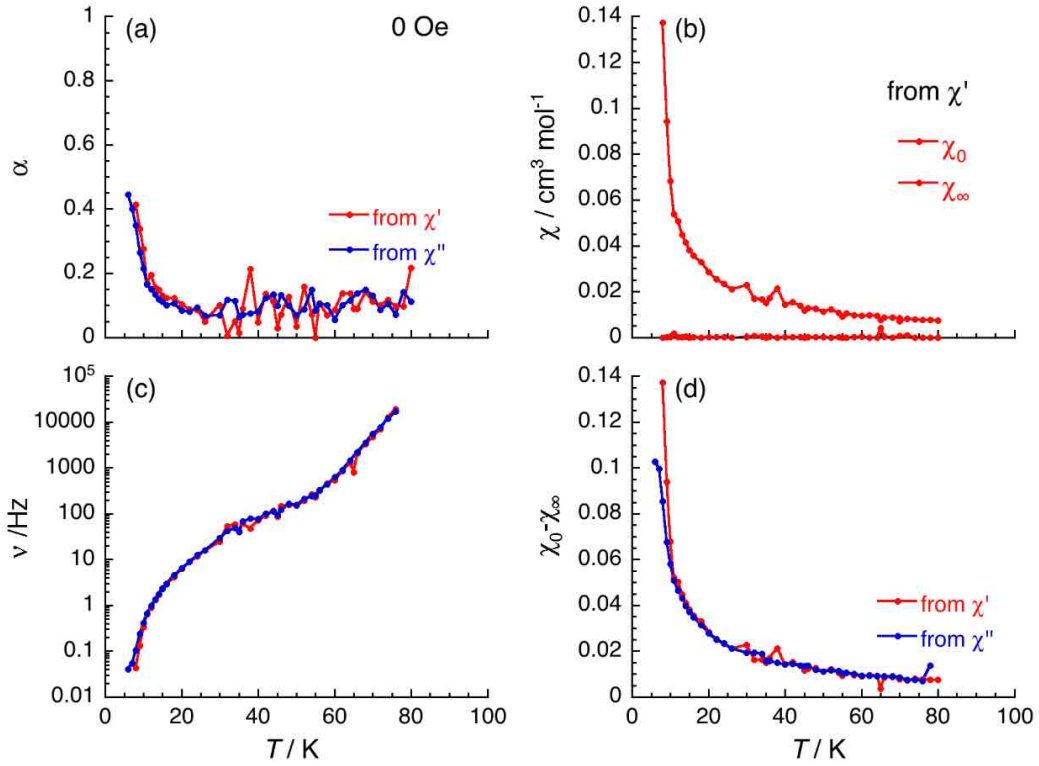

Figure S40. Field dependence of the parameters, α, ν, χ_0, χ_∞ and χ_0-χ_∞, between 1.85 and 86 K in zero-dc field deduced from the generalised Debye fit of the frequency dependence of the real (χ') and imaginary (χ'') components of the ac susceptibility shown in Figure S39, for **5%Dy@1-Y**.

Table S11 Recent selected top eight compounds with highest activation energy values and their relaxation parameters. (T_B is given for a 100 s characteristic time).

	Δ/k_B (K)	τ_0 (10^{-12} s)	C (s^{-1} K^{-n})	n	τ_{Raman}^{30K} (s)	τ_{QTM} (s)	T_B^{100s} (K)	Ref.
$[Dy(Cp(Me)_5)(Cp(^iPr)_5)][B(C_6F_5)_4]$	2217	4.2	3.1×10^{-8}	3	1195	25000	65	[14]
$[Dy\{Cp(^iPr)_4(Me)\}_2][B(C_6F_5)_4]$	2112	4.01	1.57×10^{-6}	2.07	558	2452	62	[15]
$[Dy\{Cp(^iPr)_5\}_2][B(C_6F_5)_4]$	1919	11.8	8.04×10^{-7}	2.31	481	1187	59	[15]
$[Dy(Cp^{ttt})_2][B(C_6F_5)_4]$	1760	19.9	1.66×10^{-6}	2.15	402	—	53	[16]
$[Dy\{Cp(^iPr)_4(Et)\}_2][B(C_6F_5)_4]$	1986	7.79	3.36×10^{-8}	3.02	1030	447	59	[15]
$[Dy\{Cp(^iPr)_4\}_2][B(C_6F_5)_4]$	1848	3.39	2.27×10^{-5}	2	49	439	17	[15]
$[Dy(O^tBu)_2(py)_5][BPh_4]$	1815	1.17	1.0×10^{-6}	3.77	2.7	—	12	[17]
$[Dy\{P(CtBuCMe)_2\}_2][Al\{OC(CF_3)_3\}_4]$	1760	2.0	3.1×10^{-4}	1.1	77	—	24	[18]

8. References:

[1] S. K. Sur, *J. Magn. Reson.* **1989**, *82*, 169–173.

[2] D. F. Evans, *J. Chem. Soc.* **1959**, 2003.

[3] Agilent, *Technol. UK Ltd, Yarnton, Oxford, UK* **2014**, *44*, 1–53.

[4] G. M. Sheldrick, *Acta Crystallogr. Sect. A Found. Crystallogr.* **2008**, *64*, 112–122.

[5] G. M. Sheldrick, *Acta Crystallogr. Sect. C Struct. Chem.* **2015**, *71*, 3–8.

[6] O. V. Dolomanov, L. J. Bourhis, R. J. Gildea, J. A. K. Howard, H. Puschmann, *J. Appl. Crystallogr.* **2009**, *42*, 339–341.

[7] L. J. Farrugia, *J. Appl. Crystallogr.* **2012**, *45*, 849–854.

[8] Persistence of Vision Raytracer (Version 3.6), **2004**.

[9] S. Alvarez, P. Alemany, D. Casanova, J. Cirera, M. Llunell, D. Avnir, *Coord. Chem. Rev.* **2005**, *249*, 1693–1708.

[10] F. Aquilante, J. Autschbach, R. K. Carlson, L. F. Chibotaru, M. G. Delcey, L. De Vico, I. Fdez. Galván, N. Ferré, L. M. Frutos, L. Gagliardi, et al., *J. Comput. Chem.* **2016**, *37*, 506–541.

[11] B. O. Roos, R. Lindh, P. Å. Malmqvist, V. Veryazov, P. O. Widmark, *J. Phys. Chem. A* **2004**, *108*, 2851–2858.

[12] B. O. Roos, R. Lindh, P.-Å. Malmqvist, V. Veryazov, P.-O. Widmark, *J. Phys. Chem. A* **2005**, *109*, 6575–6579.

[13] L. Ungur, L. F. Chibotaru, *Chem. Eur. J.* **2017**, *23*, 3708–3718.

[14] F. S. Guo, B. M. Day, Y. C. Chen, M. L. Tong, A. Mansikkamäki, R. A. Layfield, *Science* **2018**, *362*, 1400–1403.

[15] K. R. McClain, C. A. Gould, K. Chakarawet, S. J. Teat, T. J. Groshens, J. R. Long, B. G. Harvey, *Chem. Sci.* **2018**, *9*, 8492–8503.

[16] C. A. P. Goodwin, F. Ortu, D. Reta, N. F. Chilton, D. P. Mills, *Nature* **2017**, *548*, 439–442.

[17] Y. S. Ding, N. F. Chilton, R. E. P. Winpenny, Y. Z. Zheng, *Angew. Chem. Int. Ed.* **2016**, *55*, 16071–16074.

[18] P. Evans, D. Reta, G. F. S. Whitehead, N. F. Chilton, D. P. Mills, *J. Am. Chem. Soc.* **2019**, *141*, 19935–19940.